

# Realisation of full-Bloch beams with ultrafast Rabi-rotating vortices

Lorenzo Dominici,<sup>1</sup> Nina Voronova,<sup>2,3</sup> David Colas,<sup>4</sup> Antonio Gianfrate,<sup>1</sup> Amir Rahmani,<sup>5</sup> Vincenzo Ardizzone,<sup>1</sup> Dario Ballarini,<sup>1</sup> Milena De Giorgi,<sup>1</sup> Giuseppe Gigli,<sup>1</sup> Fabrice P. Laussy,<sup>6,7</sup> and Daniele Sanvitto<sup>1,8</sup>

<sup>1</sup>*CNR NANOTEC, Istituto di Nanotecnologia, Via Monteroni, 73100 Lecce, Italy*

<sup>2</sup>*National Research Nuclear University MEPhI (Moscow Engineering Physics Institute), 115409 Moscow, Russia*

<sup>3</sup>*National University of Science and Technology MISIS, 119049 Moscow, Russia*

<sup>4</sup>*ARC Centre of Excellence in Future Low-Energy Electronics Technologies, School of Mathematics and Physics, University of Queensland, St Lucia, Queensland 4072, Australia*

<sup>5</sup>*Department of Physics, Yazd University, Yazd, Iran*

<sup>6</sup>*Russian Quantum Center, Skolkovo innovation city, 121205 Moscow, Russia*

<sup>7</sup>*Faculty of Science and Engineering, University of Wolverhampton, Wulfruna Street, WV1 1LY, UK*

<sup>8</sup>*INFN sezione di Lecce, 73100 Lecce, Italy*

Strongly-coupled quantum fluids, such as multi-component atomic condensates, optical fields and polaritons, are remarkable systems that allow to test the most fundamental symmetries and conservation laws of Physics. When the coupling between the components is coherent, not only the particles number, but also their phase texture that maps the linear and angular momentum, can be exchanged. Here, using optical pulses of different topologies and their coherent control, we excite the multi-component fluid of exciton-polaritons in such a way that all quantum states on the Bloch sphere are simultaneously present and undergo a structured Rabi-oscillatory dynamics. As a result, the complex light emitted from the cavity is characterized by inner phase singularity tubes spiraling around their axis of propagation, *i.e.*, we observe a new kind of swirling vortices endowed with oscillating linear and orbital momentum, which exhibit ultrafast motion with striking accelerations beyond superluminal speed. This vortex motion is tracked by means of the stereographic projection, thanks to the created homeomorphism between the Bloch sphere and the real physical plane, and expressed in terms of the Möbius transformation.

## I. INTRODUCTION

Some of the most counter-intuitive concepts of Physics arise from the representation that quantum mechanics brings to the usual notions of reality: one cannot refer to physical objects with definite properties and attributes, but only to measurements made on them. Despite the knowledge of the wavefunction, descriptions most often remain in terms of localized objects: particles. Even when interactions between them are not weak perturbations, this interpretation in terms of objects is typically extremely robust and accurate, as one can preserve it by introducing new quasi-particles, such as the bogolons in interacting Bose gases or the so-called *polaritons*, that arise when interactions between particles become too strong, as compared to the free energy, to be considered as a perturbation. The conceptualization of quasi-particles is not reduced to the fundamental cases of interacting modes, but can also be applied to a wide family of topological defects. Solitons, for instance, that are nonlinear-wave phenomena bearing all the characteristics of physical objects, can be better and accurately described as such. Quantized vortices are another stunning example. They are the fundamental modes of rotation for fields mapped by a complex wavefunction (in particular, atomic Bose-Einstein condensates,<sup>1</sup> superfluids,<sup>2</sup> superconductors,<sup>3</sup> electron beams,<sup>4,5</sup> and light<sup>6,7</sup>). While vortices stem from a delocalized rotation in the entire space, in the hydrodynamic (long-wavelength) limit they are neatly pictured as objects localized at their core. Since the wavefunction must reconnect with itself, its phase  $\varphi$  has to undergo an integer number of twists when looping around the center of rotation. This number is called

phase winding, or topological charge, and defines the (intrinsic) orbital angular momentum (iOAM) per particle, quantized in units of  $2\pi$ . This manifests most strikingly through the so-called *vortex core*, a null-density point-like phase singularity in which the wavevector  $\mathbf{k}$  diverges (since  $\mathbf{k} = \nabla\varphi$ ). Within optical fields, the connection between the Maxwell description and quantum hydrodynamics is revealed via the so-called singular beams.<sup>8–10</sup> Their physical nature can be best recognized through the use of such angular momentum carrying objects for information processing,<sup>11,12</sup> for instance in offering a new degree of freedom for multiplexing.<sup>13,14</sup> Recently, curved light beams<sup>15</sup> and standing or moving solenoidal beams<sup>16</sup> have been proposed as the most advanced tools for optical tweezers.<sup>17,18</sup> The rich vortex-related phenomenology illustrates the importance of the recent advances with optical vortices, giving rise to the field of “complex light” or “structured light”.<sup>19</sup>

Among quantum fluids able to sustain vortices, microcavity exciton-polaritons<sup>20,21</sup> have brought forward unique assets to study these objects, including their multi-component nature with coherent coupling and their spin features.<sup>22–28</sup> One key attribute of polaritons is their so-called *Rabi oscillations*.<sup>29,30</sup> In the strong coupling regime of the two bare components—the cavity photon and the exciton fields—new normal modes of the system appear. The two eigenmodes are known as the upper (UP) and lower polariton (LP) modes, whose dispersions are separated in energy by the Rabi splitting. The polariton Rabi oscillations are known since the first polariton studies, but their sub-picosecond imaging and control have only recently been achieved.<sup>29</sup> While the vorticity transfer and dynamics in coherently coupled atomic

BECs has been considered theoretically,<sup>31,32</sup> here, based on the recent progress in both the quality of samples and the level of control and detection, we experimentally study for the first time the joint polariton Rabi-oscillatory and spatio-temporal vortex dynamics.<sup>33,34</sup> It yields the spectacular phenomenology illustrating how notions of ‘physical objects’ must be treated with care and linked to the underlying full-wavefunction picture. Namely, in the light emitted from the system, we observe a vortex, being at all times accurately defined and visible, undergoing striking and bizarre dynamics that seemingly breaks some basic laws of physics, including the periodically changing angular momentum without applied forces and going faster than the speed of light.

Experimentally, we implement a concept of orbital coherent control of microcavity exciton-polaritons based on the coherent transfer of particles and their momentum to create light structured in both space and time, so as to *carry simultaneously all three different kinds of angular momentum of an optical beam*:<sup>35</sup> the states we create are circularly polarized, which corresponds to spin angular momentum (SAM), they carry the topological charge of a vortex (iOAM) initially imprinted by the excitation, and possess an extrinsic orbital angular momentum (eOAM) brought forward from the displacement of the vortex core from the origin. Finally, their center-of-mass, the core, and the net transverse linear momentum (nTLM) are also rotating in time, endowing them with time varying OAM.<sup>36</sup> With a fine control on the sought shape and dynamics of the fields formed in the microcavity, we obtain a new state to which we will henceforth refer to as a *rartex* (a “Rabi-rotating vortex”). Theoretically, we show that we create a wavefunction that realizes simultaneously *all* the possible quantum states of the system’s Hilbert space, and the measurement being made solely on one of the projections (photons) results in such a staggering phenomenology. Since we presently focus on the simplest possible case of a two-dimensional Hilbert space, *i.e.*, of a Bloch sphere, we refer to this situation as a *full-Bloch beam*. We show how such a richly-structured object has the appropriate mathematical description, namely, a conformal and bijective link between the real plane and the Bloch sphere spaces. Moreover, while the full wavefunction total density is rigidly rotating on the Bloch sphere, its projection onto an “observable” state leads to an amazing behavior going beyond firmly established physical laws and that cannot be accounted for in any simple way. Both our physical system and its theoretical description remain at the most fundamental (linear) level without complex effects of many-body interactions or nonlinearities. In particular, we demonstrate how simple linear dissipation further adds interesting twists to an already puzzling dynamics, where the complex evolution can be represented in terms of a general Möbius transform.

The paper is organised as follows. In the next Section, we describe the experiments where a particular combination of the topology of excitation with the Rabi-

oscillatory dynamics gives rise to the peculiar dynamics mentioned above. We will first exhibit this dynamics, and then, in Section III, we provide its reproduction by the theoretical model and discuss the underlying concept that makes this complex phenomenology, while being a particular case of the Schrödinger equation, a beautiful quantum mechanical example of a projective measurement performed on the full wavefunction. In the concluding Section, we discuss the concrete consequences and impact of our findings on polaritonics in particular and on the research fields that deal with dressed states of light-matter interactions and richly structured fields, in general.

## II. THE RARTEX: A RABI-ROTATING VORTEX

### A. Initialisation and spiraling dynamics

The coherent control is performed by spatially overlapping two pulses generated externally to the sample, with and without optical vortices, delayed in time, with a fine control on the sought shape and dynamics of the wavepacket formed in the microcavity. Namely, we overlap a femtosecond Laguerre-Gauss  $LG_{00}$  laser pulse onto an  $LG_{01}$  pulse created by means of a patterned liquid crystal retarder (a  $q$ -plate).<sup>28,37</sup> The first excitation pulse (pulse  $A$ ) directly generates the polariton fluid, setting an initial condition to be a vortex state upon resonant photon-to-polariton conversion on the sample. The control pulse (pulse  $B$ ), which is vortex-free, is obtained from the unconverted part out of the  $q$ -plate. The spatial structures of pulses  $A$  and  $B$  are shown in Fig. 1a. Such maps are the photonic emission maps from the polariton fluid after an independent excitation by one of the two pulses. For simplicity, the pulses  $A$  and  $B$  are co-polarized (and chosen to be circular). In a further extension of this work, one could also realize a full Bloch-Poincaré beam by using different polarizations. The relative power between the two pulses  $P_A/P_B$  is set close to 2, in order to have a comparable top density for the associated polariton populations at the time of the control pulse arrival. The temporal delay  $t_{AB}$  between the two pulses is controlled by the difference in the two arms lengths (excitation delay line), defining the optical phase shift between the pulses  $\varphi_{AB}$  (modulo  $2\pi$ ). Finally, the photon leakage out of the cavity is monitored by the use of the digital holography technique,<sup>29</sup> based on the time-resolved (detection delay line) homodyne interference that allows us to track in time with ultrafast precision the complex-valued photon field dynamics, *i.e.*, both its phase and intensity.

In the absence of the Rabi coupling, the result would be immediate:<sup>38</sup> pulse  $B$ , the plain-Gaussian  $LG_{00}$  with a central top intensity and homogeneous phase, coherently sums up to the previous vortex field  $LG_{01}$ , which is empty in its centre. The central phase singularity is thus instantaneously displaced to a new position, by the de-

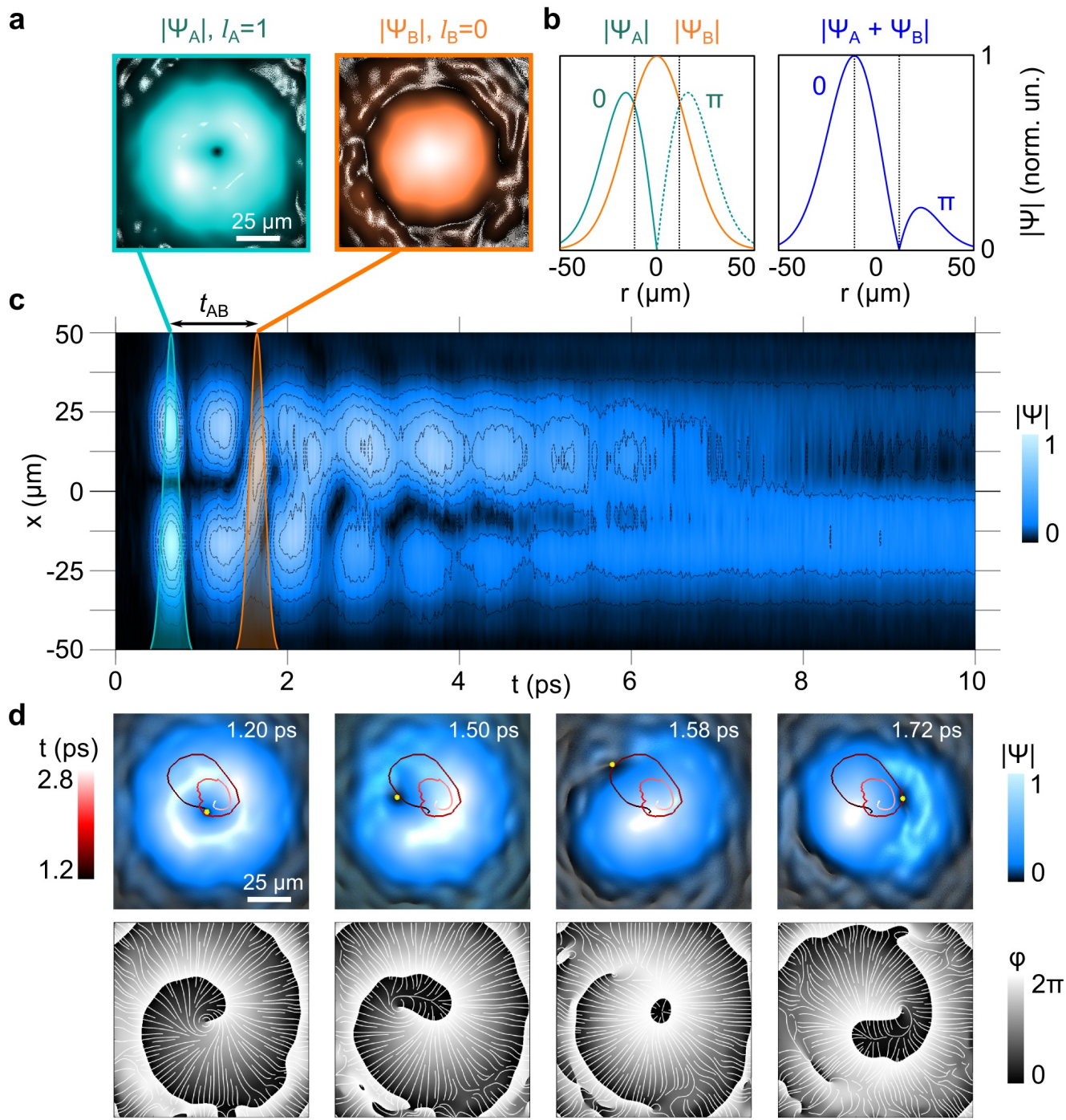


**Fig. 1. Rartex experiment.** **a**, Photonic emission from the polariton fluid excited by independent resonant pulses, either the vortex  $A$  or the plain Gaussian  $B$ . **b**, Simplified scheme to represent the displacement of the vortex core position by a coherent overlap of the beams. The solid and dashed parts of the green line, representing the profile of the pulse  $A$ , are in anti-phase. The resulting state is asymmetrical, where the new positions for both the maximum and null density (*i.e.*, vortex core) are obtained at a radial distance set by the condition of totally constructive and destructive interference (*i.e.*, where the original beams have the same intensity), respectively. **c**, Timespace charts of the polariton amplitude along a central crosscut in the double pulse experiment. The superimposed time envelopes represent the time of arrival and width of the excitation and control pulses (time delay  $t_{AB} \approx 1$  ps). Desynchronization of the Rabi oscillations along the diameter is evident in their bending after the arrival of the pulse  $B$ . **d**, Evolution of the polariton amplitude and phase. The snapshots are taken at successive moments of time  $t = 1.20, 1.50, 1.58$ , and  $1.72$  ps. The phase singularity is tracked and marked as a yellow dot in the amplitude maps, and the red curve represents its trajectory along a timespan of two Rabi periods ( $t = 1.2 - 2.8$  ps). The white streamlines in the phase maps represent the in-plane momentum vector field (retrieved as  $\mathbf{k}_C = \nabla\varphi$ ). See also the Supplementary Movie SM1.

structive interference between the initial and the newly-generated field, as sketched in Fig. 1b. In 2D, the specific direction of the displacement is set by the optical phase delay, *i.e.*, the new azimuthal position of the vortex core is set by the phase shift  $\varphi_{AB}$  between the two pulses, which is one example of a feature which we are able to control coherently with extreme accuracy. Similarly, a new density maximum is obtained in the radially opposite direction to the core. Here however, since the normal modes of the system differ from the bare cavity mode, additionally to the displacement of the vortex, the obtained composite polariton fluid is set into a very peculiar motion, with a rotation of the vortex core itself, as shown in Fig. 1c and d (cf. Supplementary Movie SM1 for better illustration of the effect). Figure 1c displays the chart of the photonic amplitude along a central crosscut, sampled with a  $\delta t = 20$  fs timestep. This chart makes evident the peculiar feature achieved by the use of a double excitation pulse with different topologies: the density imbalance along the crosscut, the filling of the empty core of the initial vortex by the second pulse, and, importantly, the desynchronization of the Rabi oscillations between the radially opposed regions. Furthermore, Fig. 1d shows the photonic amplitude and phase maps of the fluid at initial and successive moments. The initial circular symmetric  $LG_{01}$  vortex (Fig. 1d,  $t = 1.20$  ps) is suddenly displaced aside upon the arrival of the pulse  $B$  ( $t = 1.50$  ps). Soon after, it gets at the boundary of the polariton cloud ( $t = 1.58$  ps), before coming back again closer to the inner region ( $t = 1.72$  ps). The solid line in the amplitude maps shows the vortex core trajectory in the timespan of two Rabi periods ( $t = 1.2$ – $2.8$  ps). The radial damping is due to the faster UP dephasing time  $\tau_U \sim 2$  ps.<sup>29</sup> It can be roughly described as a spiraling orbit, where the full loop is travelled in a time of  $T_R = 0.78$  ps, but with a *varying speed* along the trajectory (here  $T_R = 2\pi/\Omega_R$  denotes the Rabi oscillations period). Namely, the core is seen to accelerate dramatically as it gets close to the edge of the spot and then to slow down as it re-penetrates the condensate. Note that the location of the core is easily and unambiguously tracked in the phase mapping. A similar effect, with a smaller orbit, is obtained for the photon density center-of-mass.

## B. Coherent control of the vortex lines

The trajectory of the observed vortex core is reported as  $xyt$  vortex lines in Fig. 2a, in the 0.5–10 ps time range, where the two vortex lines correspond to two different realizations, upon starting with opposite iOAM (*i.e.*, opposite initial vortices imprinted by the pulse  $A$ , either  $l_A = +1$  or  $l_A = -1$ ). When starting with opposite windings, also opposite spiraling directions (eOAM) are obtained. Additionally, the fine-delay control allows us to rotate the whole  $xyt$  core trajectory around the  $t$  axis, by changing the optical phase shift  $\varphi_{AB}$  between the two pulses. As an example, the two specific realizations cor-

responding to slightly different values  $\varphi'_{AB}$  and  $\varphi''_{AB}$  are shown in Fig. 2b, in the 0.5–6.0 ps time range. The entire set of core trajectories describes a closed  $xyt$  topological surface, upon scanning the phase shift  $\varphi_{AB}$  along one complete  $2\pi$  turn, as shown in Fig. 2c. The surface has been mapped in a limited time range (a single Rabi period, 2.0–2.8 ps) upon registering the phase singularity position (solid spheres) at regular time intervals of 0.1 ps, and by changing  $\varphi_{AB}$  by successive  $\sim \pi/4$  steps. Here the detail of a specific vortex string (blue tube sampled every 20 fs) demonstrates how the line is perfectly carved on the topological surface. It is observed that every  $xy$  encircling path that encompasses the topological surface produces a unitary phase winding, for every time into the dynamics and every value of  $\varphi_{AB}$ . The closed surface is fundamentally symmetric around the initial vortex position, and its radius breathes with the Rabi period. The circular symmetry of the surface is a direct consequence of the symmetry of both the initial vortex pulse  $A$  and the Gaussian pulse  $B$ , and of their coaxial alignment. The circular symmetry is further evident in the panels of Fig. 2d, which report the amplitude and phase of the polariton fluid at a fixed time of the dynamics ( $t = 2.6$  ps) but for different phase delays ( $\varphi_{AB}$  spaced by  $\pi/2$  intervals, which in other terms is  $\lambda/4$  length delay differences). The vortex core is at this time displaced from the centre by always the same distance, but at a changing azimuthal direction that directly maps the optical phase shift, and describes an almost perfect circle (see black/white line in the density maps Fig. 2d). The rartex line at a fixed time can also be represented in the  $xy\varphi_{AB}$  space, where it assumes the helicoidal shape, as represented in Fig. 2e.

## C. Rartex velocity and momentum

The average speed of the rartex along an orbit depends on the orbit size ( $\propto r_{\text{orbit}}$ ), as the oscillation period stays fixed by the Rabi coupling. For example, in the experiments of Fig. 1d, the photonic phase singularity is sweeping a closed  $xy$  curve with the mean radius of 20  $\mu\text{m}$  during the first Rabi loop, revealing  $\sim 150 \mu\text{m ps}^{-1}$  that is half the speed of light  $c$  in vacuum. Moreover, the vortex core speed is not constant: the largest speed is achieved when the core is far from the centre of the spot, in the orbital apex position. At the same time, the price to pay for orbits larger than the packet width is that the apex position would also correspond to a very low density peripheral background, on top of which the density dip would move. Therefore a natural question arises, regarding the maximum absolute value of velocity at which the phase singularity is pushed and can be detected during the dynamics.

For experimental realizations with slightly expanded beams sizes as compared to Fig. 1, in Fig. 3a,b we present the in-plane  $xy$  orbits of the phase singularity during the first and second Rabi loops. The circles are the instantaneous positions tracked every 20 fs, while the lines are

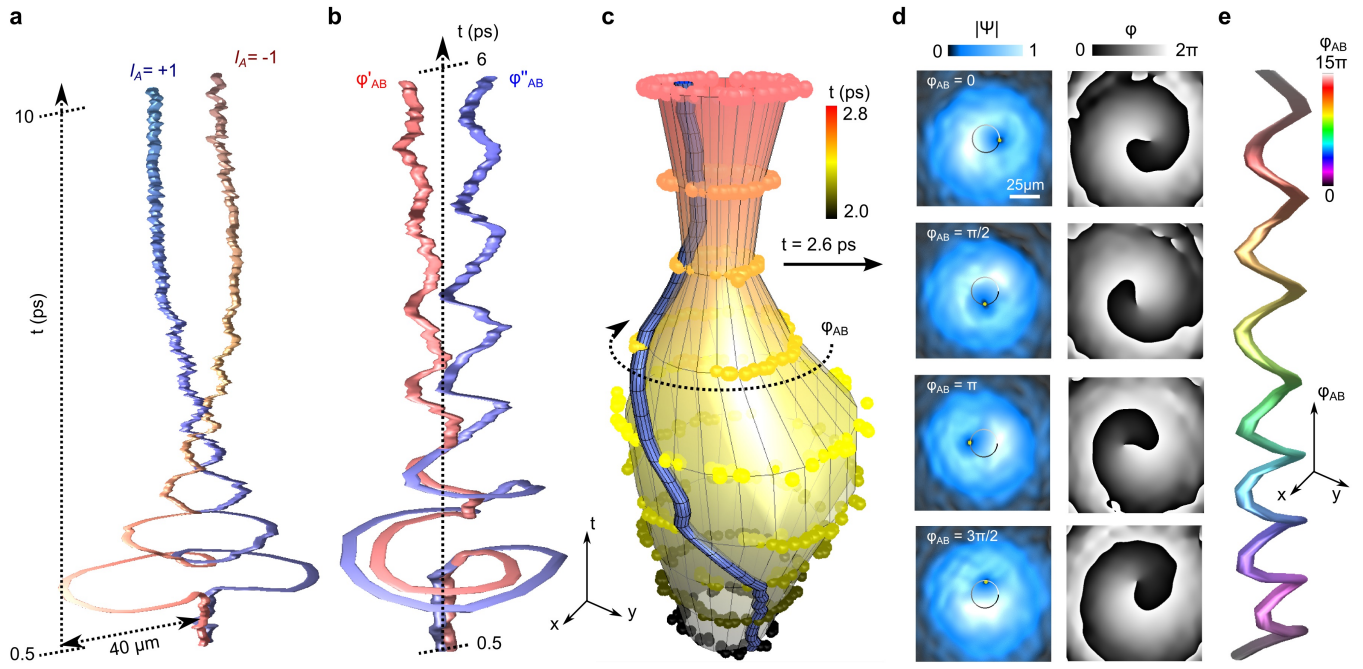


**Fig. 2. Coherent control of rartex lines.** **a**, Experimental  $xyt$  photonic vortex line (time range  $t = 0.5 - 10$  ps, step  $\delta t = 0.02$  ps). The two realizations correspond to the opposite  $l_A = +1$  (blue) and  $l_A = -1$  (red) initial topological charges, resulting in the opposite direction of spiraling of the vortex core. **b**, Experimental  $xyt$  vortex lines (time range  $t = 0.5 - 6.0$  ps) for two different optical phase shifts  $\varphi_{AB}$  between the excitation pulse  $A$  ( $LG_{01}$ ) and the control pulse  $B$  ( $LG_{00}$ ). **c**, A detail of the dynamics during a single Rabi period ( $t = 2.0 - 2.8$  ps). The bottle-envelope represents the  $xyt$  surface topology drawn by the different vortex lines when sweeping  $\varphi_{AB}$ . Its radius breathes with the Rabi oscillations. The topological surface has been mapped (spheres) at 100 fs time intervals, spanning  $\varphi_{AB}$  in a  $15\pi$  range by successive  $\sim \pi/4$  steps. The blue tube represents a specific  $xyt$  vortex line corresponding to a given  $\varphi_{AB}$ . **d**, Amplitude and phase of the polariton fluid at a fixed time of the rartex dynamics ( $t = 2.6$  ps), for different realizations corresponding to optical phase shifts spaced by  $\pi/2$ . The vortex core has been marked with a yellow dot in the amplitude maps, and the black/white line is the fitting circle to all the isotime positions of the previous panel. **e**, Helicoidal rartex string in the virtual  $xy\varphi_{AB}$  space at a fixed time.

mapping the trajectory. The integrated distance swept by the rartex core and the corresponding instantaneous velocities, retrieved from the latter, are shown in Fig. 3c,d, respectively. In all these panels, different colors represent different speed ranges of the core: subluminal speed (black), superluminal speed with respect to the cavity medium (yellow),  $v_{\text{core}} \geq c/n_{\text{cavity}} = 100 \mu\text{m ps}^{-1}$ , and superluminal speed relative to vacuum (red),  $v_{\text{core}} \geq c = 300 \mu\text{m ps}^{-1}$ . Here,  $n_{\text{cavity}} \sim 3$  is the refractive index of the photonic cavity medium. As one can see, the rartex goes well over the speed of light (twice as fast at its peak velocity) and does so cyclically with intervals where it gets almost at rest, implying drastic accelerations and decelerations. The panel Fig. 3e shows the numerically reproduced integrated distance swept by the core along a given orbit during the Rabi period, for different values of the global UP-LP population imbalance parameter  $S$  (see the next Section for details). The sigmoid shape of these curves can be approximated by an inverse tangent of time, and the corresponding experimental curve in Fig. 3c is fitted with two different inverse tangent dependencies for the first and the second Rabi loops, re-

spectively. The corresponding computed orbital speed of the core  $v_{\text{core}}$  normalized to the average speed along an orbit ( $\langle v_{\text{core}} \rangle = 2\pi r_{\text{orbit}}/T_R$ ) is shown in Fig. 3f. In both Fig. 3e and f, we are using on the horizontal axis the wrapped orbital time along a generic Rabi cycle, where  $t = 0.5T_R$  corresponds to the rartex reaching the apex position. For details of modelisation, we refer to Section III.

A complementary picture to the rartex rotational dynamics is provided by the evolution of the linear and angular momenta. Although both pulses  $A$  and  $B$  have no mean transverse linear momentum (mTLM)  $\langle \mathbf{k} \rangle = 0$ , and exactly one unit of angular momentum  $l_A = \pm 1$  from the pulse  $A$ , when the rartex is triggered, the mean linear and angular momenta of the observed photon field start to oscillate, as shown in Fig. 4a and b, respectively. In Fig. 4a, the mTLM vector  $\langle \mathbf{k}_C \rangle$  dynamics is computed from the momentum streamlines (represented in the inset of Fig. 4a for  $t = 1.5$  ps), weighted by the photon density, for successive moments of time in the range  $t = 1.5 - 3.8$  ps. The mean angular momentum evolution shown in Fig. 4b is retrieved from the measured photon complex wavefunction  $\psi_C$  via the direct integra-

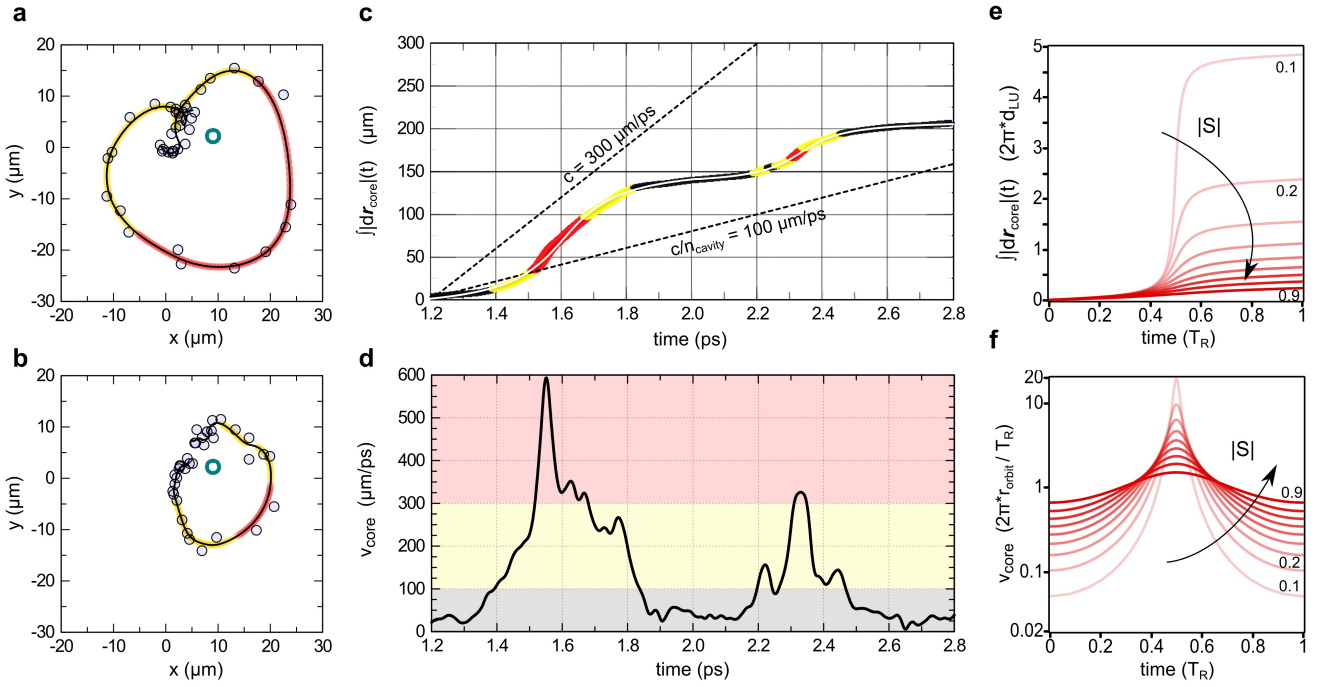


**Fig. 3. Rartex dynamics.** **a,b**, In-plane vortex core positions (grey open dots) and trajectory (color line) swept during the first (a) and second (b) Rabi loops. The three different colors shading the line represent the part of the trajectory during which the vortex core locally moves at subluminal speed (black), superluminal relatively to the cavity medium (yellow), and superluminal relative to vacuum (red). The green open dot in the centre maps the position of the LP vortex core (extracted from the experimental data by time-fitting the model interference term, see Appendix for details). **c**, Experimental integrated distance swept by the observable photonic vortex core along the trajectory during the first two Rabi cycles. The dashed lines have a slope corresponding to the speed of  $c$  and  $c/n_{\text{cavity}}$ , as a reference. The color code is the same as in a,b. The superimposed white solid line results from merging the two separate fitting of the distance by an inverse tangent during each orbital time range (1.2–2.0 and 2.0–2.8 ps). **d**, Velocity of the vortex core during the first two Rabi cycles. The color code for the background is the same as in a–c. **e**, Model integrated distance swept by the core in one Rabi cycle, for different orbits parameterized by the global content imbalance ( $S$  values ranging from 0.1 to 0.9, as marked). The distance is expressed in terms of the LP-UP core distance  $d_{LU}$  (which is a fixed quantity for a given realization). **f**, Model instantaneous velocity for the core, for different global imbalances (the color of the curves correspond to the same values of  $|S|$  as in e). The speed is normalized to the average velocity along a given orbit ( $\langle v_{\text{core}} \rangle = 2\pi r_{\text{orbit}}/T_R$ ), and it is expressed in a log scale to compress the different aspect ratios in the same panel.

tion  $\langle L_z \rangle = i \int \psi_C^* (y \partial_x - x \partial_y) \psi_C dr / \int |\psi_C|^2 dr$ . The modelling results for  $\langle \mathbf{k}_C \rangle$  and  $\langle L_z \rangle$  are presented in Fig. 4c and d, together with the respective quantities for the exciton field (see further discussion in the next Section). The observed oscillations of momenta in the light emitted from the cavity call into question the conservation laws of these physical quantities and the nature of the force and torque which rule them. In particular, such oscillations appear to corroborate and generalize recent observations of the so-called self-torque<sup>36</sup> whereupon the OAM (per particle) is evolved internally and self-consistently, being in our case furthermore periodically altered rather than changing in a monotonous way, and also manifesting a self-force that similarly drives the linear momentum.

### III. RARTEX MODELISATION AND THE FULL-BLOCH BEAM CONCEPT

The observed dynamics of the two LG beams with OAM 0 and 1 subject to Rabi oscillations, is striking: one has seemingly a photon vortex, known from a vast literature to otherwise behave as a physical object, that is seen to undergo the peculiar motion of fast accelerations and decelerations along circular orbits, overtaking the speed of light in the process. It is known that phase velocity can be superluminal, especially within interference phenomena,<sup>39</sup> but it appears counter-intuitive that a vortex would stop providing a useful and valid physical picture to describe the dynamics of the system. If it does still provide such a picture, how can one account for it and what are the conservation laws, *e.g.*, ruling the time-varying angular momentum of a quantized vortex that is itself in orbital motion? Superluminal motion of

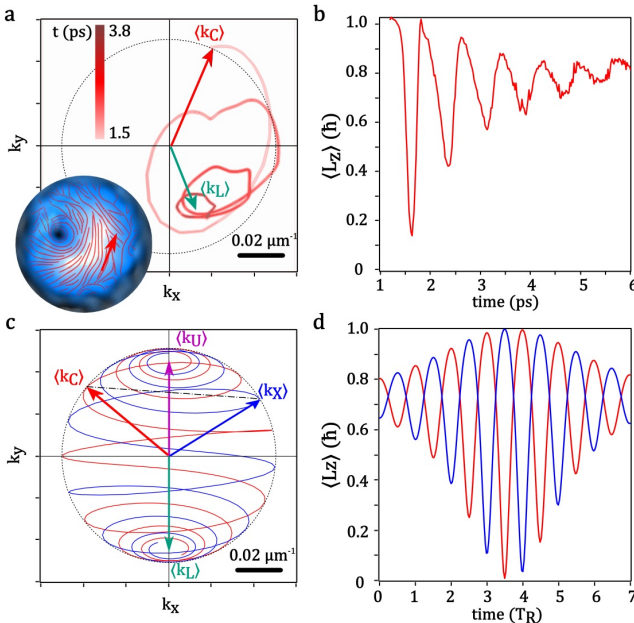


**Fig. 4. Linear and angular momentum evolution.** **a**, Experimental mean transverse linear momentum  $\langle \mathbf{k}_C \rangle$  (per particle) in the photon field during time (red arrow and red line, time range 1.5 to 3.8 ps). The  $\langle \mathbf{k}_L \rangle$  (green vector) represents the in-plane vector momentum of the LP mode (extrapolated as the limit vector of the photonic one). The inset shows the density map overlaid with the streamlines of momentum corresponding to the azimuthal gradient of the phase at  $t = 1.50$  ps (for the full gradient  $\mathbf{k}_C = \nabla\varphi$ , see the maps in Fig. 1d). **b**, Experimental OAM (per particle) with respect to the central origin (*i.e.*, the center of the initial  $LG_01$  pulse). Panels **a**,**b** are relative to the same experimental realization as presented in Fig. 1. **c**, Model transverse mean linear momentum vectors in the four components,  $\langle \mathbf{k}_{U,L,X,C} \rangle$ . The momenta in the normal modes are fixed and pointing upwards and downwards because the vortex cores in these fields are displaced to the left and right, respectively. The total momentum  $\langle \mathbf{k} \rangle$  keeps always vertical, drifting from  $\langle \mathbf{k}_U \rangle$  to  $\langle \mathbf{k}_L \rangle$  in time due to differential decay. The linear momenta in the bare fields oscillate, in such a way that their vectorial sum is always instantaneously null in the horizontal direction. Their vertical components are instead oscillating around the shifting vector  $\langle \mathbf{k} \rangle$ . **d**, Mean orbital angular momentum in the photon (red) and exciton (blue) field with respect to the initial centered axis of symmetry. Both **c**,**d** are modeled for a situation of  $\pi$ -opposite displacement of the UP and LP vortex cores, with the initial and final conditions  $S = +0.98$  and  $S = -0.98$ , respectively, and  $\Omega_R/\gamma_R = 10$ .

a physical object has been previously discussed,<sup>39,40</sup> typically in experiments performed in the region of anomalous dispersion of an absorbing material and in tunneling experiments,<sup>39</sup> or upon proper space-time shaping of a wavepacket,<sup>40</sup> neither of which however is the case for polaritons. Here we propose an explanation which clarifies the above questions.

### A. Homeomorphic mapping between real space and the Bloch sphere

Our first observation is that the dynamics of the rartex that arises from the interplay of coherent coupling and vorticity can be reproduced with the standard coupled Schrödinger equations (cSEs) that accommodate these two ingredients. The cSEs are written for the coupled exciton  $\psi_X(x, y, t)$  and photon  $\psi_C(x, y, t)$  macroscopic wavefunctions (see Appendix); hence, while only the photonic field  $\psi_C$  is easily accessible in the experiments, the theory allows us to study as well the excitonic component  $\psi_X$ , and the LP(UP) fields  $\psi_{L,U} = (\psi_C \pm \psi_X)/\sqrt{2}$  (in the simplest case of zero detuning), or any other combination of those.

Assuming at first the particle-conserving model with no decay terms, we show in Fig. 5a the position of the vortex cores in both  $\psi_C$  (red), corresponding to the one measured experimentally, and  $\psi_X$  (blue) as functions of time, along with the vortex cores in LP (UP) in green (purple), all of which are easily computed as the null-density points (phase singularities) of the respective wavefunctions. The excitation pulse  $A$  creates a preset condition with the vortex perfectly centered into the beam, and *coincident* in all four fields. Upon arrival of the control pulse  $B$ , the  $\psi_U$  and  $\psi_L$  vortices appear *split* into fixed positions out of the center of the beam, being separated by the distance  $d_{LU}$ , as shown in Fig. 5a, b, and c. As described above, the direction of the instantaneous displacement of the vortex core should be defined by the time delay between the pulses  $t_{AB}$ . Here, since the normal modes of the system have different well-defined eigenenergies  $\hbar\omega_{U,L}$ , the respective optical phase shifts  $\varphi_{AB}$  between the two pulses for the UP and LP fields differ:  $\varphi_{AB}^{U,L} = 2\pi(t_{AB} \bmod t_{opt}^{U,L})/t_{opt}^{U,L}$ , where  $t_{opt}^{U,L} = 2\pi/\omega_{U,L}$ . Thus the angular difference between the directions of displacement of the UP and LP vortices  $\varphi_{AB}^U - \varphi_{AB}^L$  becomes defined by the coarse time-delay between the two pulses (of the order of the Rabi period  $T_R$ , in the ps scale) and hence by the associated Rabi phase  $\Phi_{AB} = 2\pi(t_{AB} \bmod T_R)/T_R$ . The UP-LP cores displacement directions are opposite and hence  $d_{LU}$  is maximal (as shown in Fig. 5a, b, and c) when the pulse  $B$  is sent in the so-called anti-Rabi-phase (*i.e.*,  $t_{AB}$  is an half-integer multiple of  $T_R$ ); on the contrary, if  $t_{AB}$  is an integer multiple of  $T_R$  (the two pulses are in Rabi-phase), the  $\psi_{U,L}$  vortices are displaced to the same point in space. The two leftmost panels in Fig. 5g show the UP and LP cores displacement for the experimental realization of Fig. 3, where the UP and LP density profiles were reproduced from the measured photon wavefunction using the time-fitting of the experimental data with the normal modes interference model at each position (see Appendix for details of the experimental data fitting, and for additional modelisation cases of various time delays).

The displacement of the UP and LP vortices to different positions results in the non-coinciding spatial profiles of the two eigenstates  $\psi_{U,L} = |\psi_{U,L}|e^{i\varphi_{U,L}}$  (as schemati-

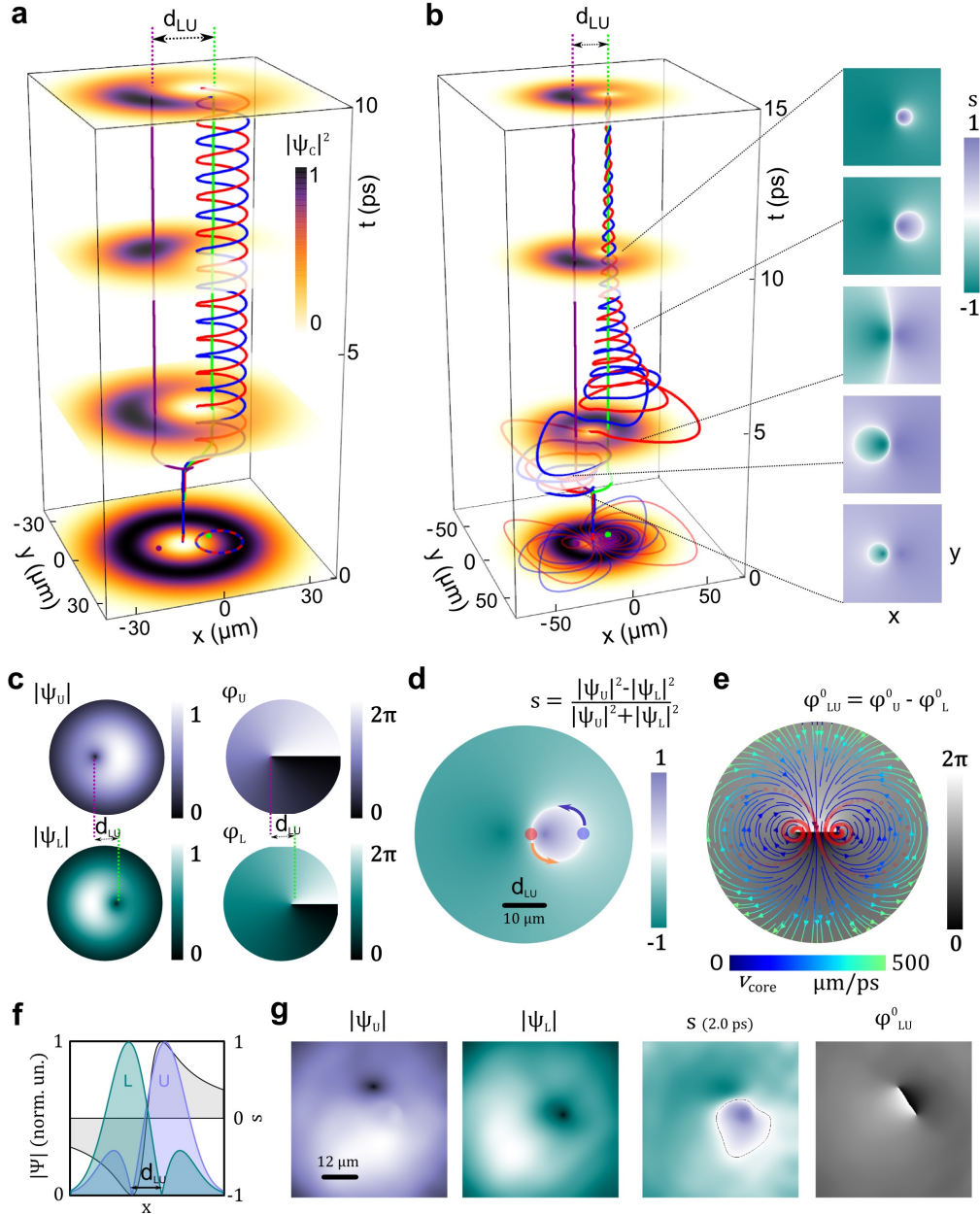


**Fig. 5. Rartex numerics, model and data modes decomposition.** **a,b**, Numerical  $xyt$  vortex lines (purple in the UP mode, green the LP, red the photon, blue the exciton). Photonic density  $|\psi_c(x,y)|^2$  maps are superimposed at selected time frames. The preset condition from the pulse  $A$  provides coinciding vortex cores in all of the fields. Upon arrival of the pulse  $B$ , the four cores are displaced to different positions. In **a**, the decay is set to zero and the system is excited closer to the LP energy. In **b**, the system is excited closer to the UP energy and features the UP dephasing  $\gamma_U = 0.2 \text{ ps}^{-1}$ . The photon and exciton cores first circle around the UP line, while the global UP-LP relative content  $S$  changes, resulting in the orbit radius growth, and then switch to rotation around the LP vortex core, finally shrinking as the UP population leaves the system. The slow change of the instantaneous orbits in time due to the UP dephasing is shown in the local polariton imbalance parameter  $s = (|\psi_U|^2 - |\psi_L|^2) / (|\psi_U|^2 + |\psi_L|^2)$  maps on the right, where the white string indicates the isodensity line  $s = 0$  at each chosen moment of time (a circular orbit with drifting centre and radius). **c**, Maps of the amplitudes and phases of the normal modes, revealing the displacement of the UP and LP vortices and the density asymmetry inside each of the two modes. **d**, Spatial distribution of the local polariton imbalance  $s$  in the case LP > UP content in the system (*i.e.*, global imbalance  $S < 0$ ), as in **a**. The photon and exciton cores (red and blues dots) move along the orbit of UP-LP isodensity line  $s = 0$ . **e**, Spatial distribution of the relative phase  $\varphi_{LU}^0$ , which is that of a vortex dipole. The photon core movement (red dots) follows the direction of the gradient  $\nabla\varphi_{LU}^0$  (shown by streamlines). The color of the streamlines represents the core velocities, larger at the boundary:  $v_{\text{core}} = \Omega_R / |\nabla\varphi_{LU}^0|$ . **f**, Simplified scheme to represent the non-coinciding profiles in the LP and UP fields due to the vortices being split by the distance  $d_{LU}$ , top views of which are given in **c**. The right axis shows the changing local imbalance parameter  $s$  across the cut, for the case of global UP/LP populations being equal ( $S = 0$ ). **g**, Left to right: experimental maps (the realization of Fig. 3) corresponding to theoretical panels **c**, **d**, and **e**, obtained by time-fitting the measured photon density with the interference model at each point  $(x, y)$ .

cally represented in Fig. 5f) and, as a consequence, in an instantaneous change of the ratio  $|\psi_U|/|\psi_L|$  and the phase difference  $\varphi_{LU} = \varphi_U - \varphi_L$  at each point in space. Effectively, it means that the polariton fluid at each position  $(x, y)$  is now characterized by its own relative content and relative phase between the upper and the lower polariton, changing from one point to the other. As can be seen in the upper part of Fig. 5a, at the arrival of the second pulse and this instantaneous excitation of the whole majority of linear combinations of  $\psi_U$  and  $\psi_L$  within the spot, the vortex cores in the coherently coupled bare fields  $\psi_{C,X} = (\psi_U \pm \psi_L)/\sqrt{2}$  (being one example of such linear combinations) start to describe circular orbits. At every instant, the exciton and photon cores are on the  $\pi$ -opposite relative phase positions along the orbit, thus acting similarly to a Newton's cradle, with one core slowing down while the other one accelerates. The varying speeds of the cores are well visible in the vortex lines (see also the Supplementary Movies SM1 and SM2): despite being perfect circles when projected on the  $(x, y)$ -plane, the  $\psi_{C,X}$  vortices cores orbits in Fig. 5a are not perfectly helical in  $xyt$  space.

Our second observation is that there is a privileged geometry to describe the rartex phenomenon, and this is not the 2D plane (in real or reciprocal, *i.e.*, Fourier-transformed, space) where a continuous mapping of multiple wavefunctions ( $\psi_{C,X,L,U}$ ) should be done at each time interval. Instead, the best way to describe the system's intricate dynamics is on the polariton Bloch sphere.<sup>29</sup> Each quantum state (QS) of the system can be expressed through the complex wavefunctions of the two eigenstates on this sphere, as follows:

$$|QS\rangle = \frac{1}{\sqrt{2}}(\sqrt{1-s}|L\rangle + \sqrt{1+s}e^{i\varphi_{LU}}|U\rangle), \quad (1)$$

where  $|L\rangle$  and  $|U\rangle$ , being the pure LP and UP states, correspond to the south and north poles of the sphere, respectively. The sphere radius is normalised to the total polariton density  $|\Psi_{total}|^2 = |\psi_L|^2 + |\psi_U|^2$ , and we introduced the parameter  $s = (|\psi_U|^2 - |\psi_L|^2)/(|\psi_U|^2 + |\psi_L|^2)$ , representing the *local* (position-dependent) UP-LP population imbalance. The representation of the Bloch sphere and its metrics is given in the upper panel of Fig. 6a. Since the values of  $s$  effectively define the latitude on the surface of the Bloch sphere (being exactly the projection on the vertical LP-UP axis), it can be seen as an analogue to the Stokes parameter  $S_3$  on the Poincaré sphere of polarizations. Thus, each QS is uniquely identified by a point with the coordinates  $(s, \varphi_{LU})$ . When the bare energies of the photon and exciton states are equal (no detuning), the Rabi-oscillatory dynamics corresponds to the rigid rotation of the Bloch sphere around the vertical axis (see the three rows of Fig. 6a), so that in the absence of decay, the parameter  $s$  stays fixed in time, and the temporal evolution of each QS is governed by the azimuthal angle changing continuously as  $\varphi_{LU} = \varphi_{LU}^0(\mathbf{r}) + \Omega_R t$ , *i.e.* the sum of the geometrical and dynamical phases, respectively. As discussed above, the spatial component

of the relative phase  $\varphi_{LU}^0(\mathbf{r})$  is not uniform in space, but has the shape of an UP-LP vortex dipole defined by the UP and LP spatial profiles, which is shown in Fig. 5e (model) and f (experiment). The spatio-temporal evolution  $\varphi_{LU}(\mathbf{r}, t)$  is provided in the Supplementary Movie SM3. Neglecting the spread in momentum on the dispersion relation, which is a good approximation for broad-enough wavepackets over the Rabi timescale, one can assume all states to follow the same equator-parallel dynamics (*i.e.*, the QS trajectories are defined by the equation  $s(x, y) = \text{const}$ , see Fig. 6a and the corresponding lines in the real space in Fig. 6b). This treatment allows, first of all, to easily track the trajectories of the photon and exciton vortices cores by looking for the trajectories where  $s(x, y) = 0$ , since the points of zero-density in the respective fields  $\psi_{C,X}$  are bound to move along the lines where  $|\psi_U|^2 - |\psi_L|^2 = 0$ , which corresponds to the equator of the Bloch sphere (see Fig. 5d showing the distribution of  $s$  in space, and the line marked as  $s = 0.0$  in Fig. 6c that shows the photon wavefunction). Second and more importantly, the description (1) provides a correct way to express the *full* wavefunction of the system, both as a function of real plane coordinates  $(x, y)$  and the Bloch sphere angles  $(s, \varphi_{LU})$ , which now cannot be limited to  $\psi_{C,X}$  or  $\psi_{L,U}$  alone.

The nature of the state which is actually created in the experiment can now be revealed: by superimposing two pulses and displacing the vortices in the normal modes of the system, one realizes a *full-Bloch beam*, in the sense that all quantum states of the Bloch sphere (all values  $-1 \leq s \leq 1$  and  $0 \leq \varphi_{LU} < 2\pi$ ), except just one specific state at each moment of time (see below), are simultaneously present somewhere in the physical space. Since each point in space realizes a different QS, the measurement of the “photon field” is made on the position-dependent fraction of the polariton fluid, hence the measured photon wavefunction is given by  $\psi_C(x, y, t) = |\Psi_{total}(x, y)|\langle x, y|\Psi_C^{\text{pr}}\rangle$ , where the projection of different quantum states onto the photon state of the Bloch sphere is given by

$$|\Psi_C^{\text{pr}}\rangle = |C\rangle\langle C|QS\rangle = \frac{1}{2}(\sqrt{1-s} + \sqrt{1+s}e^{i\varphi_{LU}})|C\rangle \quad (2)$$

with  $s = s(x, y)$ ,  $\varphi_{LU} = \varphi_{LU}(x, y, t)$ , and  $|C\rangle$  being normalized to unity. A similar expression can be obtained for the “exciton field” by projecting the QS in each point of space on the exciton state:  $|X\rangle\langle X|QS\rangle$ . From this perspective, the observed vortex core corresponds to the QS of the polariton Bloch sphere, which, when projected onto a photon state according to Eq. (2), provides a null-density, *i.e.*,  $|\Psi_C^{\text{pr}}\rangle = 0$ , whereas  $|\Psi_{total}|$  stays non-zero (while the neighbouring points create a phase singularity). Clearly, the photon vortex core corresponds to the  $|X\rangle$  state on the sphere: by definition, this state has no photon component and is therefore the only point where  $|\Psi_C^{\text{pr}}\rangle$  vanishes. Any other QS has a nonzero photon content, so the singularity is indeed reduced to a single point. Similarly, the exciton vortex core corresponds to

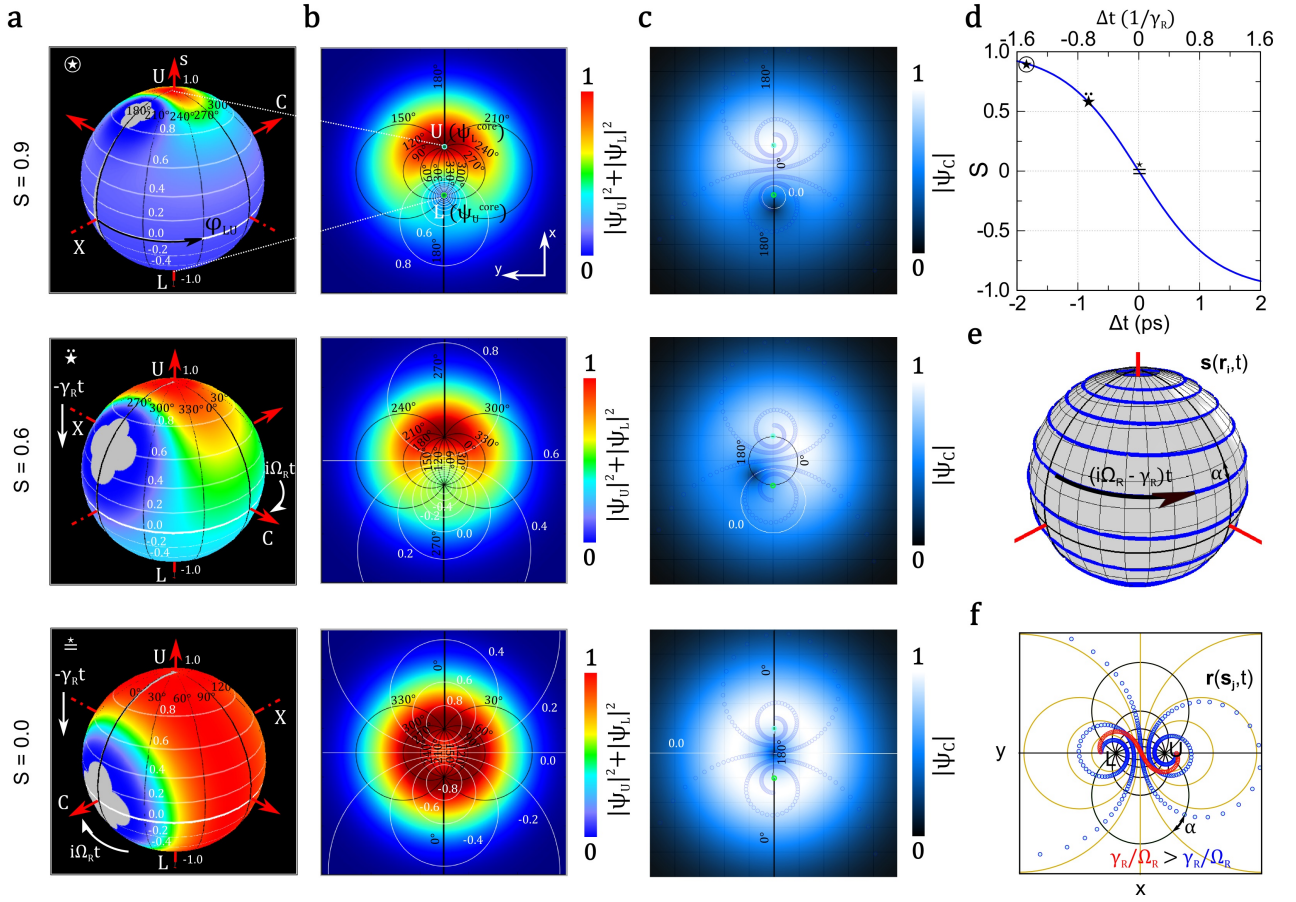


**Fig. 6. The Bloch sphere metric and its homeomorphism to real space.** **a**, The full-Bloch beam and its dynamics are shown by plotting the normalized (with respect to the maximum value) total density  $|\Psi_{total}|^2 = |\psi_U|^2 + |\psi_L|^2$  on the Bloch sphere. The sphere metric consists of white parallels and black meridians. The Rabi oscillations are associated with the rotation of the sphere in time ( $i\Omega_R t$ ) around the vertical axis. The three panels (top to bottom) correspond to three different values of  $S = 0.9, 0.6, \text{ and } 0.0$ , which, in the conservative case, is set by the excitation. With the differential decay taken into account, the three panels correspond to three successive moments of time separated by  $1.25T_R$ , while the decay in time ( $-\gamma_R t$ ) is associated to the  $|\Psi_{total}|^2$  density drift downwards along the vertical axis. **b**, The stereographic projection of the total density to the real space  $|\Psi_{total}(x, y)|^2$ . The reshaping of the total density on the  $(x, y)$ -plane is not affected by the Rabi rotation, but only by the differential decay. The two families of mutually orthogonal Apollonian circles, marked as white and black lines, map the loci of isocontent  $s$  and isophase  $\varphi_{LU}$  degree of freedom, respectively. The isophase circles swap with each other in a progressive manner due to Rabi oscillations (as  $\varphi_{LU}$  grows linearly with time), while the isocontent circles drift due to decay. See the Supplementary Movies SM3 and SM4 for better visualisation. **c**, The corresponding profiles of the photon wavefunction  $\psi_C(x, y)$ , obtained by applying the projection operation (2) to the full wavefunction  $\Psi$ . The white line shows the isocontent  $s = 0$ , being the trajectory of the photon vortex core in space, while its intersection with the isophase  $\varphi_{LU} = \pi$  gives the exact position of the core (corresponding to the  $|X\rangle$  state on the sphere). The superimposed double spiral shows the overall trajectory of the photon vortex in the presence of the decay, starting from  $S = 0.9$ . For **a-c**,  $\gamma_R/\Omega_R = 0.1$ . **d**, The global UP-LP content ratio  $S(t)$  evolution due to the decay. The curve can be started in any of its points, depending on the initial condition  $S(0)$  defined by the excitation, thus here it is represented versus the time delay  $\Delta t$  symmetrically with respect to the point  $S = 0$ , at which the UP and LP populations are equal. The same curve is followed locally by the parameter  $s(\mathbf{r}, t)$  at each point of the real space, starting from different values according to the initial distribution  $s(\mathbf{r}_i, 0)$ . The three successive moments of the dynamics shown in the rows of panels for the total density on the Bloch sphere (**a**) and in real space (**b**) correspond to the three points along this curve  $S(t)$ , as marked. **e**, The Bloch-sphere trajectory  $\mathbf{s}(\mathbf{r}_i, t)$  (blue curve) of a QS in the presence of the decay, for a given real space point  $\mathbf{r}_i$  (one chosen QS), for  $\gamma_R/\Omega_R = 0.05$ . Here, the vector  $\mathbf{s}$  defining the QS on the sphere combines the two spherical coordinates  $\{s, \varphi_{LU}\}$ . **f**, Trajectories  $\mathbf{r}(\mathbf{s}_i, t)$  (blue and red dots) of a specific QS in real space, on top of the Bloch conformal metric that consists of two family of circles: the yellow circles of the stereonet represent the isodensity orbits with drifting centre and radius at different times (see also the Supplementary Movie SM4), while the black circles show the isophase lines delimiting the sectors equally spanned in time during the Rabi loops, in total 9 orbits (parameter  $S$  from -0.8 to 0.8 stepped by  $\delta S = 0.2$ , plus the UP and LP cores,  $S = \pm 1$ ) and 12 isophase lines (stepped by  $\delta\varphi_{LU} = \pi/6$ ). For the blue curve,  $\gamma_R/\Omega_R = 0.1$  as in **a-c**, while for the red curve  $\gamma_R/\Omega_R = 0.5$ . The rhumb angle with respect to the isocontent parallels is defined by  $\tan \alpha = \gamma_R/\Omega_R$  both on the sphere (**e**) and in real space (**f**). Note that the panels **b** are rotated by  $90^\circ$  compared to **f**, for a clearer correspondence with the Bloch sphere shown in **a**.

the point where  $|QS\rangle = |C\rangle$ . In fact, the rartex topology is such that any point in space becomes a vortex core in a certain basis of observables.

The excitation of different quantum states in each point of space creates a homeomorphic mapping between the 2D Bloch sphere of quantum states and the 2D real-space physical plane (including infinity), as shown in Fig. 6a, b. The metric consisting of parallels and meridians on the sphere is conformally (*i.e.*, angle preserving) matched by the metric made of two mutually orthogonal circle families, or bipolar circular coordinates (Apollonian circles) in real space (see in Fig. 6b, where the constant  $s$  and  $\varphi_{LU}$  are marked by the white and black lines, respectively). This physical realization of a mathematical homeomorphism between the extended complex plane (here:  $(x, y)$ -plane plus a point at infinity) and the Riemann sphere (here: the polariton Bloch sphere) results in a stereographic projection that maps circles on the sphere to circular trajectories on the plane, except the projection point associated with the QS that is at infinity in real space. Due to the Rabi rotation, this QS is not a fixed point on the sphere, but a changing one. The projection plane (the  $(x, y)$ -plane shown in Fig. 6b and c) is at all times tangent to the sphere on the opposite side from the projection point. In all panels of Fig. 6a, the projection point on the Bloch sphere is the QS exactly in the middle of the grey area; at the same moment of time, the QS which is  $\pi$ -opposite to it on the sphere (on the same parallel) is projected to real space exactly in the middle of the UP-LP vortex dipole in the relative phase profile  $\varphi_{LU}(x, y; t)$ . This effect is best illustrated in the bottom row of the panels Fig. 6a–c: when the projection point on the Bloch sphere coincides with the state  $|C\rangle$ , the  $\pi$ -opposite state (*i.e.*,  $|X\rangle$ ) corresponds to the photon vortex core which is seen in (c) exactly in the middle between the stereoprojections of the points  $|U\rangle$  and  $|L\rangle$ . The position of the projection point and hence the exact shape of the stereographic projection from the Bloch sphere to the plane are defined by the *global* imbalance of the UP and LP populations in the system, namely,  $S = \int(|\psi_U|^2 - |\psi_L|^2)dr / \int(|\psi_U|^2 + |\psi_L|^2)dr$ . The three rows in Fig. 6a, b, and c, corresponding to three different values of  $S$ , show the snapshots of the total density  $|\Psi_{total}|^2$  distribution on the Bloch sphere, the stereographically-projected  $|\Psi_{total}(x, y)|^2$  distribution in real space, and the corresponding profile of the photon wavefunction  $|\psi_C(x, y)|$  obtained by the QS-projection according to (2), respectively. Only in the case of equal total populations  $S = 0$  (bottom row), the parallels  $s = \text{const}$  are projected symmetrically to the  $(x, y)$ -plane (see the schematic representation of this case in Fig. 5f). The equator of the sphere and hence the trajectory of the  $\psi_{C,X}$  vortex cores in this case is projected to a straight line going to infinity exactly in the middle of the UP-LP vortex dipole, symmetrically dividing the trajectories corresponding to parallels from the upper and the lower semi-spheres on the  $(x, y)$ -plane (see the bottom panels in Fig. 6b and c). However, when the system is excited

closer to the UP energy ( $0 < S < 1$ ), the projections of all parallels (the isodensity lines) shift toward the opposite semi-space, forming circles around the  $\psi_U$  core (point ‘L’ on the real plane), as shown in the top two rows of Fig. 6b, and around the LP core (point ‘U’) when excited closer to the LP energy ( $-1 < S < 0$ ). Examples of cSEs dynamics in different cases, depending on the excitation energy, are presented in Fig. 5a, b (together with the interference model maps of  $s(x, y)$ ), and Appendix.

The evolution of any QS, including the photon and the exciton vortices cores which belong to the sphere equator, can now be described as transformations of the extended complex plane, belonging to the Möbius group:<sup>41</sup>  $f(z) = (az + b)/(cz + d)$ . Associating the complex number  $z$  with the QS coordinates on the Bloch sphere as  $z = \psi_U/\psi_L = \sqrt{(1 + s)/(1 - s)} \exp\{i\varphi_{LU}\}$ , the Rabi-rotation of the sphere (alternatively, this can be seen as a rigid rotation of the total density on a motionless sphere, see Fig. 6a) yields  $a = \exp\{i\Omega_R t\}$ ,  $b = c = 0$ , and  $d = 1$ . The two fixed points of the Möbius transformation in real space are represented by the positions of the LP and UP vortex cores, which correspond to the  $|U\rangle$  and  $|L\rangle$  states on the Bloch sphere, respectively (see the points marked as ‘U’ and ‘L’ in the corresponding top panels of Fig. 6a and b). These are the only two points which cannot undergo any change, *i.e.*, being pure states, or normal modes, they preserve themselves.

Since, in the linear regime, any QS is kept on the Rabi-rotating sphere, this must be true in space as well. As a consequence, any QS, for example the pure exciton state  $|X\rangle$  (the  $\psi_C$  vortex core), which is to be found at a given location at any given time, must drift continuously to another location in space in the next instant of time, with the same intensity, following the phase gradient  $\nabla\varphi_{LU}$  (see the streamlines in Fig. 5e and the Supplementary Movie SM4). Analogously with the usual (single mode) group speed being expressed in terms of the infinitesimal differentials  $v_g = d\omega/dk$ , here one can write for the core velocity  $v_{\text{core}} = \Delta\omega/|\Delta\mathbf{k}| = (\omega_U - \omega_L)/|\mathbf{k}_U - \mathbf{k}_L| = \Omega_R/|\nabla\varphi_{LU}|$ . Hence, since the gradient streamlines for a vortex dipole are circles coinciding with the isodensity orbits  $s(x, y) = \text{const}$  (in the considered configuration of concentric LG beams of the same size), the vector expression for the core velocity has the form  $\mathbf{v}_{\text{core}} = \frac{\Omega_R}{|\nabla\varphi_{LU}|^2} \nabla\varphi_{LU}$ . The gradient  $|\nabla\varphi_{LU}|$  is larger in the middle of the vortex dipole, hence in the inner region the two moving cores are slower than at the boundary, where they move faster (see the color of the streamlines in Fig. 5e). From the geometrical point of view, because the rotation of the Bloch (Riemann) sphere corresponds to inversion (*elliptical* Möbius transform), such a drift that is a uniform on the sphere, when projected on the plane, suffers the typical Möbius stretch of circles, which is the reason for the greatly varying velocities with drastic accelerations and decelerations of the vortex core (or of any chosen QS).

The correct description of the system is therefore in terms of the full wavefunction  $\Psi(x, y, t) =$

$|\Psi_{total}(x, y)|\langle x, y|QS\rangle$  (where  $|QS\rangle(t)$  is simply rotating in time), rather than in terms of any single-component field. In fact, any “field” is a projection of  $\Psi$  onto a certain observable basis, which can indeed host superluminal artifacts. The rartex is thus a real-world implementation of the famous *superluminal scissor*. Just as the meeting point of two closing blades can go faster than the speed of light, not being an actual physical object, the core in the projected photon field  $\langle x, y|C\rangle\langle C|QS\rangle$  (see Eq. (2)), which arises from the underlying full-Bloch beam, is similarly a contrived meeting point of the polariton Hilbert space eigenstates—the upper and lower polaritons (the counterparts of the scissors upper and lower blades)—being out-of-phase. When they are in-phase, they similarly contrive to render the excitonic core instead, by projecting  $\langle x, y|X\rangle\langle X|QS\rangle$ .

## B. Differential decay and the orbits properties

To describe the full dynamics including the evolution of the global imbalance parameter  $S$ , we include the UP and LP mode decays<sup>29</sup>  $\gamma_{U,L}$ , respectively, to the cSEs model (see Appendix). Figure 5b shows the numerical dynamics of the  $\psi_{C,X,L,U}$  cores obtained for  $\gamma_U = 0.2 \text{ ps}^{-1} \gg \gamma_L$ , with the excitation and control pulses whose energy is set close to the UP mode, while the three rows of Fig. 6a–c show the different QS trajectories on the plane and on the sphere (the isodensity circular orbits) for the early times of the dynamics at the three successive moments correspondent to  $S = 0.9$ ,  $S = 0.6$ , and  $S = 0$  (top to bottom). The local imbalance map  $s(x, y)$  and the isodensity circular orbits change in time due to the reshaping of the total density on the Bloch sphere with the change of  $S(t)$ , and the trajectory of the two cores  $s(x, y) = 0$  (corresponding to a local equality  $|\psi_U|^2 = |\psi_L|^2$ ) can be seen as a “domain wall” between the areas of excess of the UP and LP densities in real space ( $s > 0$  and  $s < 0$ , the upper and the lower semi-spheres on the Bloch sphere), as shown in the snapshots on the right-hand side in Fig. 5b, as well as on the relevant experimental snapshot in Fig. 5g. As one can see, the  $\psi_{C,X}$  vortex cores first rotate around the  $\psi_U$  core, with a growing orbit radius. When the UP population decreases to the level of the LP mode, the orbit becomes a straight line between the positions of the  $\psi_{U,L}$  cores (corresponding to the limit of a circle with infinite radius). The initial configuration hence reverts, and the  $\psi_{C,X}$  vortex cores switch to spiraling from clockwise to anticlockwise direction, around the  $\psi_L$  core now, and with the decaying orbital radius as  $S$  keeps changing. Finally, they both overlap into the position of the LP core, as this is the surviving mode at long times. For a better visualisation, we refer to the Supplementary Movie SM3. The actual vortex trajectories hence result from the orbiting along these expanding/shrinking circles, with a drifting centre. Their  $xy$ -projection is a double spiral which is shown in Fig. 5e and Fig. 6c.

Finally, it is straightforward to derive that, after the

arrival of the pulse  $B$  and the initiation of the rartex dynamics, the difference in dephasing  $\gamma_R = \gamma_U - \gamma_L \approx \gamma_U$  results in the global imbalance  $S$  changing with time as  $S(t) = \tanh\{-\gamma_R t + \text{atanh}[S(0)]\}$ , which is shown in Fig. 6d. This hyperbolic tangent curve can be started at any point  $S(0)$  that is set by tuning the initial excitation energy between  $\hbar\omega_U$  and  $\hbar\omega_L$ . The decay alone, resulting in the decrease of  $S(t)$  with time, can be seen as the motion of the total density  $|\Psi_{total}|^2$  downwards along the surface of the Bloch sphere, as represented in successive panels (top to bottom) of Fig. 6a. Similarly to the rotation of the sphere, which belongs to the *elliptic* subclass of the Möbius transformations, the dynamics produced by different decay rates of the two normal modes can be seen as the dilation of the sphere, thus corresponding to the *hyperbolic* subclass of the Möbius group.<sup>41</sup> Like the elliptic transformation, the hyperbolic transformation fixes two points (in our physical case, the same points ‘U’ and ‘L’, *i.e.*, the positions of the lower polariton and upper polariton vortex cores, respectively, in real space), however the corresponding trajectories of the QS on the plane would create a family of circular arcs, along which the points flow away from the first fixed point (U) and towards the second one (L). When united together, the Rabi-rotation of the Bloch sphere and its dilation due to the differential decay create yet another type of continuous transformation that is called the *loxodromic* Möbius transform (in terms of the previously defined complex-variable function  $f(z) = (az + b)/(cz + d)$ , it is described by  $a = \exp\{i\Omega_R - \gamma_R\}t\}$ , and  $b = c = 0$ ,  $d = 1$ , as before). Under such a transformation, the resulting trajectories on the Bloch (Riemann) sphere form a family of loxodromes (rhumb lines), an example of which is shown in Fig. 6e for the QS evolution in a given arbitrary point in space  $\mathbf{r}_i$ . The corresponding trajectories of quantum states on the  $(x, y)$ -plane are double logarithmic spirals (*spira mirabilis*) in the bipolar circular coordinates  $(s, \varphi_{LU})$ , pointing away from the point ‘U’ and towards the point ‘L’, with the slope of the spiral depending on the decay to Rabi frequency ratio  $\gamma_R/\Omega_R$ , providing a circle for  $\gamma_R = 0$ . The rhumb angle with respect to the isocontent parallels is precisely defined by  $\tan \alpha = \gamma_R/\Omega_R$  both on the sphere and in real space, due to conformal mapping. Figure 6f shows the trajectories of a given QS (defined by a fixed Bloch sphere unit vector  $\mathbf{s}_i = \{s, \varphi_{LU}^0\}$ ), for two values of the ratio  $\gamma_R/\Omega_R$ . With time, all states follow this evolution towards the longer surviving LP normal mode (thus the total density shifts to the south of the sphere); at the same time, each point of the real space increases its LP content, so that the isodensity lines ( $s = \text{const}$ ) stereographic projections shift from the region around the point ‘L’ towards the point ‘U’. Finally, when the vortex cores in all fields coincide in the fixed position of the LP core, the pure UP state acquires zero density.

### C. Time-varying momentum

We can now come back to complete the description of the experimental findings, in order to account for the interesting evolution of the linear and angular momenta of the multi-component polariton fluid. The displacement of the vortices in the LP and UP components from the origin corresponds to a non-zero net linear momentum in each component, which results in the oscillations of the mean TLM and the mean OAM of the bare photon and exciton fields (as reported for photons in the experimental Fig. 4a, b). While no external transverse forces that would explain the rotation of the center of mass and the time varying linear and orbital momentum are applied, here one deals with a non-constant mass problem, in which each field, photon and exciton, coherently injects particles into its counterpart. The generalized Newton equation  $\mathbf{F}_{\text{ext}} = 0 = \hbar(m \mathbf{d}\mathbf{k}/dt + \mathbf{k} dm/dt)$  holds (*i.e.* inside the microcavity, in the case of no loss or dephasing, the total quantities are conserved). This is analogous as a concept to the OAM selective evaporation<sup>42</sup> recently used to increase the mean OAM and create a very large vortex in atomic BECs. Here, the coherent transfer implies the momentum exchange between the fluids, which is responsible for the periodical change of its instantaneous mean value in any of the two subsystems.

The numerical evolution of the  $\langle \mathbf{k}_{C,X} \rangle$  vector in each field is displayed in Fig. 4c. The OAM with respect to the original centre of symmetry  $\mathbf{o}$  of the beams can be expressed as  $\mathbf{L}_o = \mathbf{L}_{\text{core}} + \mathbf{r}_{\text{core}} \times \langle \mathbf{k} \rangle$ , where  $\mathbf{L}_{\text{core}}$  is the iOAM computed with respect to the moving centre of rotation, *i.e.*, the instantaneous vortex core, which remains constant and quantized, equal to the initial topological charge  $l_A$ . In contrast to that, both  $\mathbf{r}_{\text{core}}$  and  $\langle \mathbf{k} \rangle$  are oscillating, being expected to reach their maxima simultaneously (maximum net linear momentum for maximally displaced vortex core) and almost orthogonal to each other, so that their cross product will give rise to the OAM oscillations. The oscillations calculated for the complex modelled wavefunctions  $\psi_{C,X}$  by the direct averaging  $\int \psi_{C,X}^* \hat{L}_z \psi_{C,X} d\mathbf{r} / \int |\psi_{C,X}|^2 d\mathbf{r}$  are reported in Fig. 4d, and they agree with the above geometrical formula for  $\mathbf{L}_o$  when substituting mean  $\langle \mathbf{k}_{C,X} \rangle$  from Fig. 4c. The result can be understood as follows: in the assumption of the maximal ( $\pi$ ) angular displacement of the UP and LP cores, the origin  $\mathbf{o}$  is exactly in the middle of the UP-LP vortex dipole. For this reason, when the  $\psi_{C(X)}$  vortex core passes in between the points ‘L’ and ‘U’ (as shown in the bottom panel of Fig. 6c for the photon core), the total OAM is equal to the iOAM value  $\pm 1$ . The vortex core of the respective counterpart  $\psi_{X(C)}$  at the same moment is at infinity, which means that this field is vortex-free and its OAM is zero. All the other vortex positions result in the oscillations of  $\langle L_z \rangle$  between 0 and 1. Note that the data of Fig. 4a, b was obtained in the experimental realisation of Fig. 1, which means starting with the LP mode global imbalance ( $S \approx -0.25$ ), while the modelisation in Fig. 4c, d was performed with the initial

condition  $S(0) = 0.98$  (with decay to Rabi frequency ratio set to  $\gamma_R/\Omega_R = 0.1$ ), *i.e.*, starting very close to the UP mode, and the  $\psi_{C,X}$  vortex cores running through the whole double spiral from ‘L’ to ‘U’, changing from clockwise to anti-clockwise direction of rotation. Hence the experimental panel (Fig. 4b) needs to be compared only to the right half of the numerical panel (Fig. 4d).

The reported oscillations represent a general class of time-varying OAM, similar to the recently reported self-torque feature of light.<sup>36</sup> Here however the OAM (per particle) is assuming non-integer values in a periodical fashion, rather than changing continuously. We thus demonstrate the experimental creation of OAM fractional values (associated with displaced, off-axis vortex cores) with ultrafast oscillations (associated with the swirling core position) in the light emitted from the polariton system. Furthermore, we likewise evidence the time variations of the TLM vector, whose amplitude and direction both oscillate and swirl due to the same core radial and azimuthal motions. We point out that the associated features of the so-called self-torque (and here also self-force), are as matter of fact generated inside the device where light is linearly and coherently interacting with matter (excitons): the underlying picture is that of the Rabi-rotation of the full Bloch beam, being projected on the photon field  $\psi_C(x, y, t)$  at the moment when the photon escapes the cavity to propagate to the CCD camera (in case of Ref.,<sup>36</sup> instead, it is a nonlinear phenomenon). Despite the fact that each photon, once being emitted, is not changing its momentum, and that its motion in the longitudinal propagation direction is at the speed of light, such photonic emission could be used to drive another physical system<sup>43</sup> (*e.g.*, an atomic BEC or optically trapped nanoparticles) and to study its response to such a faster-than-light stimulus. It would be also interesting to devise the entity of angular momentum transfer<sup>44</sup> to an external system swept by our spiraling vortices.

## IV. CONCLUSIONS AND OUTLOOK

We have observed the dynamics of vortices in multi-component Rabi-coupled fluids, and shown how the interplay of Rabi oscillations and vorticity, here named “rartex”, exhibits ultrafast (and superluminal) spiraling vortex core motions with striking acceleration and deceleration. This observation is understood as the result of a complex projection of the full wavefunction which undergoes a uniform Rabi-rotational motion on the Bloch sphere that results in a greatly-varying velocity motion on the plane (also in circles). As such, the vortex core in the photon field follows a contrived dynamics similar to synchronized flashlights which can be made to travel faster than the speed of light, where the carrier of this superluminal propagation is none of the flashlights themselves. In the case of the rartex, a very peculiar configuration is created whereby all the quantum

states of the polariton Hilbert space are simultaneously present in the system, and mapped throughout the beam in such a way as to be furthermore present only at a single point. We call such a peculiar state a full-Bloch beam. This extends the concept of a full Poincaré beam<sup>45</sup> that similarly realizes all states of polarization in space, by involving the quantum dynamics (here the Rabi rotation), whose effect is precisely to create the observed dynamics for the photon core that is just one particular quantum state, namely, the pure exciton. The description in terms of uncoupled and steady upper and lower polaritonic fields overlooks that the two polariton fields are related in such a way as to exhibit all possible quantum states (their superpositions), implying nontrivial relationships of their amplitudes and phases in space and time. Furthermore, by creating such a peculiar state we realize, on a physical system, the abstract mathematical notion of a homeomorphism between the real physical  $(x, y)$ -plane (including infinity) and the polariton Bloch sphere of quantum states. The metric of parallels and meridians on the sphere is conformally linked to the plane metric of bipolar circular coordinates, or Apollonian circles. The excitation of the whole Hilbert space of quantum states is a necessary and sufficient condition for the creation of such a homeomorphism, that in turn allows to classify all the trajectories of quantum states, including vortex cores, in any basis of observables, by means of the Möbius transformation, and track them even analytically through the stereographic projection between the sphere and the plane.

This illustrates how physical interpretations in terms of familiar objects, in this case photons, which are being ultimately detected, may fail. Once emitted by the cavity, photons represent a physical field carrying an optical vortex at any time, which, from one snapshot to the next, does travel superluminally, but this effect does not originate from a photon field inside the cavity, as inside the device (*i.e.*, prior to the measurement) no such field exists: at all times, the pure photon state is represented by only one point in space. As a consequence, any physical observable that is based on the dynamics of vortices in polariton fields (or any coupled multi-component fields, in general) should be taken with caution, and one should turn to the full wavefunction description instead. Our results also provide an extremely simple and fundamental illustration of the breakdown of the physical picture which could help understand more complicated cases and serve as a textbook elementary paradigm of emergent objects acquiring their own special rules (such as entanglement arises from a full-wavefunction description broken onto a particles picture). In particular, obvious extensions of our results include going beyond the homeomorphic mapping, for instance by spreading significantly the wavefunction in momentum space so as to overlap various Rabi rotations of the Bloch sphere (higher order Rabi-rotating vortices), which results in the creation of rartices and antirartices and thus extends even further the phenomenologies of these pseudo-objects which arise

from the breakdown of the usual picture. Also, a moving rartex, interactions, and non-Gaussian states, in particular nonlocality, would definitely also impart the rartex with worthwhile additional phenomenologies. These are the topics of further work.

## ACKNOWLEDGMENTS

We would like to thank Romuald Houdré and Alberto Bramati for the microcavity sample, Lorenzo Marrucci and Bruno Piccirillo for the  $q$ -plate devices, and Carlos Sánchez Muñoz, Anton Nalitov and Alexander Romanov for fruitful discussions. We acknowledge the ERC project POLAFLOW (Grant 308136), the Italian MIUR project Beyond Nano, the Australian Research Council centre of excellence FLEET, the Russian Foundation for Basic Research (Project No. 19-02-00793), and the MINECO under contract FIS2015-64951-R (CLIQUE) for financial support.

## APPENDIX

### A. Experimental methods

The excitation laser is a 80 MHz train of 130 fs pulses with a 8 nm bandwidth properly tuned in order to resonantly excite both the LP and UP branches (with their central  $k = 0$  states respectively located at 836.2 and 833.2 nm in our sample), which is mandatory to trigger Rabi oscillations. The modes splitting of 3 nm (5.4 meV) corresponds to the Rabi period of  $T_R = 0.780$  ps. Once imprinted, the polariton vortices are left free to evolve. We operate in the intensity/density regime weak enough in order not to perturb the vortex dynamics by the nonlinearities, and in a clean area of the sample so to avoid any unintentional effects from the disorder. The positional stability of the vortex is indeed observed in the dynamics (in absence of the second/displacing pulse), during the whole LP lifetime (whose decay time is  $\tau_L \sim 10$  ps), with typical Rabi oscillations (quenching with the UP dephasing time  $\tau_U \sim 2$  ps). Standard beam splitters (BS) and  $\lambda/4$  plates are used to separate the beams, control the polarization and put them together before sending onto the sample.

In the off-axis digital holography, the resonant emission is let to interfere on an imaging camera with a time-delayed reference beam (detection delay line). The reference pulse is expanded by passing through a pinhole in order to make it wide and homogeneous. Hence, we apply digital Fourier-space filtering to retrieve both the amplitude and phase of the photon wavefunction. Customized software allows us to monitor and adjust the dynamics in real-time during this operation. The polarization can be simply postselected on the detection side by using  $\lambda/4$  or  $\lambda/2$  plates and a polarizing beam-splitter.

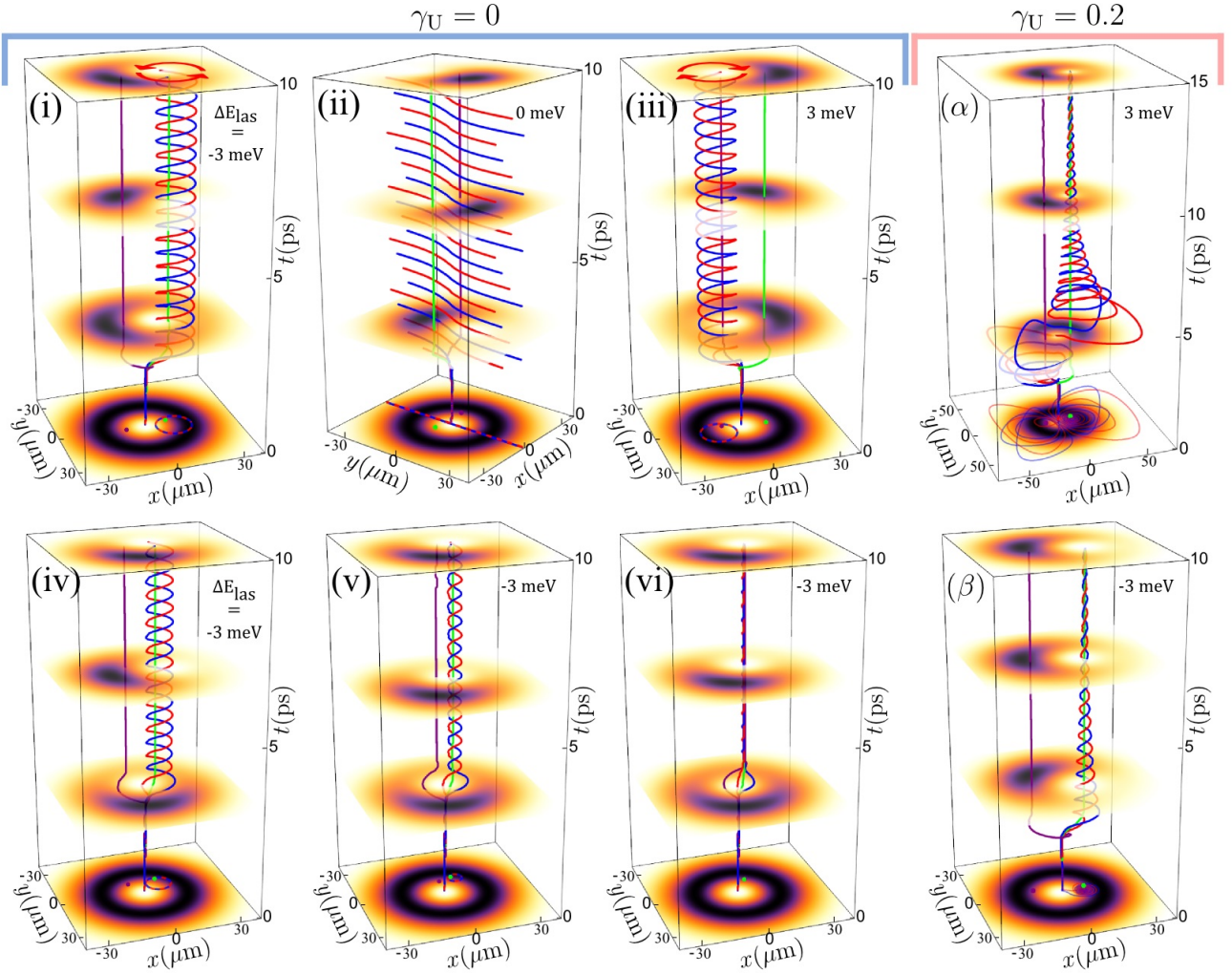


**Fig. 7. Rartex modelisation with respect to different key parameters.** **i-iii**,  $xyt$  vortex lines for photon (red), exciton (blue), UP (purple), LP (green) fields, in the absence of damping ( $\gamma_U = 0$ ), plotted for  $E_{\text{las}} = \hbar\omega_{\text{las}}$  detuned from the bottom of the bare fields dispersions by  $\Delta E_{\text{las}} = -3, 0$ , and  $3 \text{ meV}$ , which corresponds to the initial values of the global UP-LP imbalance  $S \approx -0.75, 0$ , and  $0.75$ , respectively. **iv-vi**, Vortex lines at a fixed excitation energy detuning  $\Delta E_{\text{las}} = -3 \text{ meV}$  ( $S(0) \approx -0.75$ ) for three different time delays  $t_{AB}$  between the two excitation pulses, corresponding to the successive increase of the optical phase shift  $\varphi_{AB}$  from the anti-Rabi phase (see **i** where the UP-LP cores splitting is maximal) up to the Rabi-phase where the UP and LP cores are displaced into the coinciding position (**iv**).  **$\alpha, \beta$** , Simulations with the realistic dissipation rate ( $\gamma_U = 0.2 \text{ ps}^{-1}$ ) included in cSEs model according to Eq. (4). In  **$\alpha$** , the system is initialized with a larger UP content ( $S(0) \approx 0.75$ ), so that the photon and exciton vortices start to rotate around the UP vortex core (purple line). Upon the population reversal due to the faster UP decay, at the moment when  $S(t) = 0$ , the vortices switch to rotating around the LP core (green line) in the latter part of the dynamics, thus repeating the behaviour shown in  **$\beta$** , where the excitation energy is closer to the LP mode ( $S(0) \approx -0.75$ ). See also the Supplementary Movie SM2.

## B. The coupled Schrödinger equations model

We write the two coupled Schrödinger (linear) equations according to the standard model (referred to as cSEs model in the main text):

$$i\partial_t \begin{pmatrix} \psi_C \\ \psi_X \end{pmatrix} = \begin{pmatrix} -\frac{\hbar\nabla^2}{2m_C} & \frac{\Omega_R}{2} \\ \frac{\Omega_R}{2} & -\frac{\hbar\nabla^2}{2m_X} \end{pmatrix} \begin{pmatrix} \psi_C \\ \psi_X \end{pmatrix} + \mathbf{F}, \quad (3)$$

where the photonic and excitonic fields  $\psi_{C,X}(x, y, t)$ , described by the two parabolic dispersions with effective masses  $m_{C,X}$ , are coupled via the Rabi coupling term  $\Omega_R$ . The excitation scheme is accounted for through the vector  $\mathbf{F} = (LG_{01}\mathcal{T}_A + LG_{00}\mathcal{T}_B, 0)^T$ , acting only on the photonic component. The  $LG_{01}$  and  $LG_{00}$  functions describe the vortex and vortex-free spatial shapes of the two pulses. The functions  $\mathcal{T}_{A,B} = e^{-(t-t_{A,B})^2/2\sigma_t^2} e^{-i\omega_{\text{las}}t}$  describe the pulsed time shapes, where the laser pulses are sent at the different times  $t_{A,B}$ , with the same en-

ergy  $\hbar\omega_{\text{las}}$  and temporal spread  $\sigma_t$ . The resulting motions of the vortex cores, obtained by tracking the null-density points in the photon and exciton components  $\psi_{C,X}$  and the LP and UP fields  $\psi_{L,U} = (\psi_C \pm \psi_X)/\sqrt{2}$  in space and time, are presented in Fig. 7i–vi and the Supplementary Movie SM2. The first three panels (i–iii) show the modelisation cases of different detunings of the excitation energy  $\hbar\omega_{\text{las}}$  from of the coinciding bottoms of the bare photon and exciton dispersions. Then the system is excited closer to the LP energy, that corresponds to the global prevailing of the lower polariton population, *i.e.*,  $S < 0$  (in case of Fig. 7i which coincides with Fig. 5a in the main text,  $S \approx -0.75$ ), the equator of the polariton Bloch sphere (isodensity line  $|\psi_C| = |\psi_X|$ ) is projected on the plane closer to the  $|U\rangle$  state, thus the photon and exciton cores start to describe circular orbits around the fixed position of the LP core. In the case of a fully symmetric excitation  $S = 0$ , shown in Fig. 7ii, this circle becomes a straight line exactly in the middle between the UP and LP cores positions (corresponding to the limit of a circle with an infinite radius). Finally, Fig. 7iii displays the case of the excitation closer to the UP mode ( $S \approx 0.75$ ), in which the C and X cores orbit lies closer to the projection of the  $|L\rangle$  state onto the plane, *i.e.*, around the UP core. The panels (iv)–(vi) show the modelisation results for a fixed value of  $\omega_{\text{las}}$ , closer to the LP energy, but for different time delays  $t_{AB}$  between the  $LG_{01}$  and  $LG_{00}$  pulses. One can see that with the increased delay, the angular difference between the displacements of the UP and LP cores changes, that results in the overlap of all cores positions in the case  $t_{AB}$  is equal to an integer number of the Rabi periods  $2\pi/\Omega_R$  (see Fig. 7vi).

The term  $\gamma_U \gg \gamma_L$  accounting for the UP lifetime<sup>29</sup> can be introduced in Eqs. 3, once written in the polariton basis by diagonalisation:

$$\tilde{H} = \begin{pmatrix} E_L & 0 \\ 0 & E_U - i\gamma_U \end{pmatrix}. \quad (4)$$

One can come back to the photon/exciton basis by applying the eigenvector matrix  $P$  of the original Hamiltonian:  $H = P\tilde{H}P^{-1}$ . As a result, one can plot similarly to the lossless case the  $xyt$  vortex lines for the four fields, as show in Fig. 7 $\alpha$  and  $\beta$ . The top panel ( $\alpha$ , coinciding with Fig. 5b in the main text) shows the case of the excitation closer to the UP energy and the  $\psi_{C,X}$  vortices undergoing a double spiral, first rotating clockwise around the UP core and then anti-clockwise around the LP core. The bottom panel ( $\beta$ ) shows the dynamics after the excitation closer to the LP energy, which corresponds to the experimental case of Fig. 1 of the main text.

### C. Model interference term

Within the Rabi interference model, we can express the photon density in each spatial point in terms of a mean value and a modulation term between the two bare

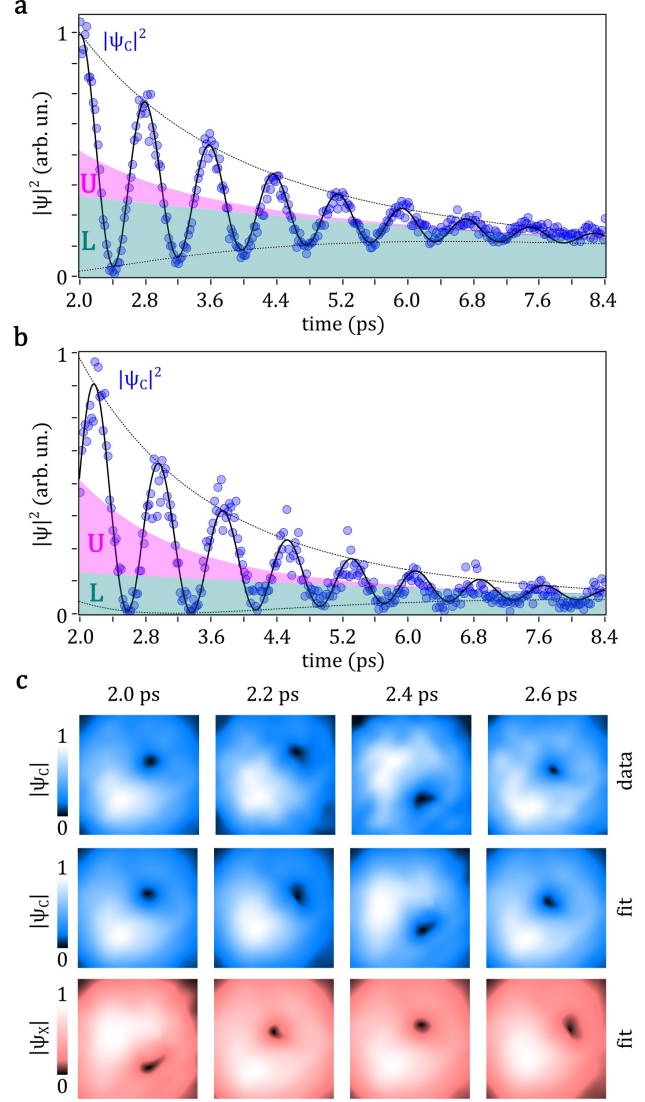


**Fig. 8. Model interference term.** **a,b** The experimental oscillations of the photon density (blue dots) and their fitting by means of the Rabi interference model (black solid line), at two different space locations (from the same realization of Fig. 3a–d and Fig. 5g). The two space locations feature opposite initial local polariton imbalance ( $s < 0$  and  $s > 0$ , respectively) and quadrature initial relative phase ( $\varphi_{LU}^0 = 0$ , and  $-\pi/2$ , respectively). The purple and green filled area represent the instantaneous UP and LP densities, respectively. **c**, The original photon density map is shown (first row) together with the interference model which is let run after the fitting in both its photon (second row) and exciton (third row) components, and at four different times.

modes, as follows:

$$|\psi_C|^2 = |\psi_L|^2 + |\psi_U|^2 + 2|\psi_L||\psi_U| \cos(\varphi_{LU}^0 + \Omega_R t). \quad (5)$$

The UP and LP modes decay is included in (5) as  $|\psi_{U,L}(t)| = |\psi_{U,L}(0)| \exp\{-\gamma_{U,L}t\}$ , providing the full temporal dependence in addition to the Rabi-oscillatory

dynamics. With the fixed experimental values for  $\gamma_U$ ,  $\gamma_L$ , and  $\Omega_R$ , and treating  $|\psi_L(\mathbf{r}, 0)|$ ,  $|\psi_U(\mathbf{r}, 0)|$ , and  $\varphi_{LU}^0(\mathbf{r})$  as fitting parameters, we fit in time the above dependence at each point  $(x, y)$  of the spot with the experimental data obtained for the photon wavefunction  $\psi_C$ , in order to retrieve the density profiles of the UP and LP polariton fields, as well as their relative phase spatial profile presented in Fig. 5g. In a similar fashion, the position of the LP core shown in Fig. 3a and b, is calculated from the experimental data by the fitting of Eq. (5). The third panel in Fig. 5g is obtained by inserting the fitted  $|\psi_L|$  and  $|\psi_U|$  at  $t = 2.0$  ps into the definition for the local UP-LP imbalance parameter:  $s = (|\psi_U|^2 - |\psi_L|^2) / (|\psi_U|^2 + |\psi_L|^2)$ . An example of time fitting (black solid lines) the photon density (blue dots) according to Eq. 5 is shown in Fig. 8a, b at different spatial positions that feature different initial local imbalance  $s(0)$  ( $s(0) < 0$  and  $s(0) > 0$ , respectively) and different  $\varphi_{LU}^0$  ( $\varphi_{LU}^0 = 0$  and  $-\pi/2$ , respectively). The fitting is performed along eight Rabi periods in the time range 2.0 to 8.4 ps, which is starting from the second Rabi cycle, *i.e.*, after the setting sequence of both pulse *A* and *B*. The comparison of the fitting dynamics with the experimental data are shown in Fig. 8c, at four times into the second Rabi cycle.

#### D. Captions to Supplementary Movies

**Movie SM1** Experimental rartex dynamics as in Fig. 1. Photonic amplitude and phase in a  $100\text{ }\mu\text{m} \times 100\text{ }\mu\text{m}$  area, with 20 fs time step. The Gaussian beam *B* is arriving at around  $t = 1.6$  ps. The vortex core position is marked with a yellow dot in the amplitude map.

**Movie SM2** Rartex dynamics simulated by the cSEs model associated to different parameters, and arranged in the same order as in Fig. 7. The  $xyt$  vortex lines for each subfield  $\psi_{C,X,U,L}$  are shown (red, blue, purple and green line for the photon, the exciton, the upper and the lower mode, respectively). The  $xy$  photonic density maps are shown at  $t = 0$  and current time planes of each graph.

**Movie SM3** The interference model showing the maps and dynamics of four relevant quantities, namely the local imbalance  $s(\mathbf{r}, t)$  and the relative phase  $\varphi_{LU}(\mathbf{r}, t)$  on the top row (blue-green map and black and white map, as in Fig. 5d,e), and the photon and exciton densities  $|\psi_{C,X}(\mathbf{r}, t)|$  (blue, red) in the second row. The fixed blue and green dots mark the fixed in space UP and LP cores, respectively. The drifting white and black circles overlapped to the photon and exciton densities represent the  $s = 0$  isocontent line and the  $\varphi_{LU} = 0 \cup \varphi_{LU} = \pi$  isophase lines, respectively. Their crossing points mark the moving photon and exciton cores (dark spots in the respective fields). The global polariton content is changing from  $S = 0.93$  to  $S = -0.9$ .

**Movie SM4** The interference model showing the evolution of the total density map  $|\Psi_{total}|^2 = |\psi_U|^2 + |\psi_L|^2$  on the left panel. The overlapped bipolar coordinates map the Bloch quantum state, *i.e.*, the polariton isocontent  $s = \text{const}$  (white circles) and isophase  $\varphi_{LU} = \text{const}$  (black circles) lines, as in Fig. 6a. The panel on the right shows the photon density in time, overlapped with a few specific  $s = 0$  isocontent lines (white) and the  $\varphi_{LU} = 0 \cup \varphi_{LU} = \pi$  circles (black). The color streamlines represent the vector velocity field of the core (and of any of the other quantum states) changing in time, retrieved from the relative phase gradient  $\mathbf{v}_{\text{core}} = \frac{\Omega_R}{|\nabla\varphi_{LU}|^2} \nabla\varphi_{LU}$ , same as in Fig. 5e.

## REFERENCES

- [1] Matthews, M. R. *et al.* Vortices in a Bose-Einstein Condensate. *Phys. Rev. Lett.* **83**, 2498–2501 (1999).
- [2] Leggett, A. J. Superfluidity. *Rev. Mod. Phys.* **71**, S318–S323 (1999).
- [3] Blatter, G., Feigel'man, M. V., Geshkenbein, V. B., Larkin, A. I. & Vinokur, V. M. Vortices in high-temperature superconductors. *Rev. Mod. Phys.* **66**, 1125–1388 (1994).
- [4] Grillo, V. *et al.* Holographic Generation of Highly Twisted Electron Beams. *Phys. Rev. Lett.* **114**, 034801 (2015).
- [5] Uchida, M. & Tonomura, A. Generation of electron beams carrying orbital angular momentum. *Nature* **464**, 737–739 (2010).
- [6] Yao, A. M. & Padgett, M. J. Orbital angular momentum: origins, behavior and applications. *Adv. Opt. Photonics* **3**, 161 (2011).
- [7] Molina-Terriza, G., Torres, J. P. & Torner, L. Twisted photons. *Nat. Phys.* **3**, 305–310 (2007).
- [8] Willner, A. E., Wang, J. & Huang, H. A Different Angle on Light Communications. *Science* **337**, 655–656 (2012).
- [9] Franke-Arnold, S., Allen, L. & Padgett, M. Advances in optical angular momentum. *Laser Photon. Rev.* **2**, 299–313 (2008).
- [10] Shen, Y. *et al.* Optical vortices 30 years on: OAM manipulation from topological charge to multiple singularities. *Light: Science & Applications* **8**, 90 (2019).
- [11] Nagali, E. *et al.* Optimal quantum cloning of orbital angular momentum photon qubits through Hong-Ou-Mandel coalescence. *Nat. Photon.* **3**, 720–723 (2009).
- [12] Leach, J. *et al.* Quantum Correlations in Optical Angle-Orbital Angular Momentum Variables. *Science* **329**, 662–665 (2010).
- [13] Wang, J. *et al.* Terabit free-space data transmission employing orbital angular momentum multiplexing. *Nat. Photon.* **6**, 488–496 (2012).
- [14] Gibson, G. *et al.* Free-space information transfer using light beams carrying orbital angular momentum. *Opt. Express* **12**, 5448 (2004).
- [15] Zhao, J. *et al.* Curved singular beams for three-dimensional particle manipulation. *Sci. Rep.* **5**, 12086 (2015).
- [16] Lee, S.-H., Roichman, Y. & Grier, D. G. Optical solenoid beams. *Opt. Express* **18**, 6988 (2010).

[17] Padgett, M. & Bowman, R. Tweezers with a twist. *Nat. Photon.* **5**, 343–348 (2011).

[18] Rahman, M. M. *et al.* Tractor beam for fully immersed multiple objects: Long distance pulling, trapping, and rotation with a single optical set-up. *Ann. Phys. (Berlin)* **527**, 777–793 (2015).

[19] Secor, J., Alfano, R. & Ashrafi, S. *Complex Light* (IOP Publishing, 2016).

[20] Kavokin, A. V., Baumberg, J. J., Malpuech, G. & Laussy, F. P. *Microcavities*. Series on Semiconductor Science and Technology (Oxford University Press, Oxford, 2017).

[21] Byrnes, T., Kim, N. Y. & Yamamoto, Y. Exciton-polariton condensates. *Nat. Phys.* 803–813 (2014).

[22] Rubo, Y. Half vortices in exciton polariton condensates. *Phys. Rev. Lett.* **99**, 106401 (2007).

[23] Lagoudakis, K. G. *et al.* Observation of half-quantum vortices in an exciton-polariton condensate. *Science* **326**, 974–976 (2009).

[24] Roumpos, G. *et al.* Single vortex-antivortex pair in an exciton-polariton condensate. *Nat. Phys.* **7**, 129–133 (2011).

[25] Voronova, N. S. & Lozovik, Y. E. Excitons in cores of exciton-polariton vortices. *Phys. Rev. B* **86**, 195305 (2012).

[26] Dall, R. *et al.* Creation of orbital angular momentum states with chiral polaritonic lenses. *Phys. Rev. Lett.* **113**, 200404 (2014).

[27] Kartashov, Y. V. & Zezyulin, D. A. Rotating patterns in polariton condensates in ring-shaped potentials under a bichromatic pump. *Opt. Lett.* **44**, 4805 (2019).

[28] Dominici, L. *et al.* Vortex and half-vortex dynamics in a nonlinear spinor quantum fluid. *Sci. Adv.* **1**, e1500807 (2015).

[29] Dominici, L. *et al.* Ultrafast control and Rabi oscillations of polaritons. *Phys. Rev. Lett.* **113**, 226401 (2014).

[30] Colas, D. *et al.* Polarization shaping of Poincaré beams by polariton oscillations. *Light Sci. Appl.* **4**, e350 (2015).

[31] Calderaro, L., Fetter, A. L., Massignan, P. & Wittek, P. Vortex dynamics in coherently coupled Bose-Einstein condensates. *Phys. Rev. A* **95**, 023605 (2017).

[32] Tylutki, M., Pitaevskii, L. P., Recati, A. & Stringari, S. Confinement and precession of vortex pairs in coherently coupled Bose-Einstein condensates. *Phys. Rev. A* **93**, 043623 (2016).

[33] Voronova, N., Elistratov, A. & Lozovik, Y. Detuning-controlled internal oscillations in an exciton-polariton condensate. *Phys. Rev. Lett.* **115** (2015).

[34] Rahmani, A. & Laussy, F. P. Polaritonic Rabi and Josephson Oscillations. *Sci. Rep.* **6** (2016).

[35] Bliokh, K. Y., Rodríguez-Fortuño, F. J., Nori, F. & Zayats, A. V. Spin-orbit interactions of light. *Nat. Photon.* **9**, 796–808 (2015).

[36] Rego, L. *et al.* Generation of extreme-ultraviolet beams with time-varying orbital angular momentum. *Science* **364**, eaaw9486 (2019).

[37] Cardano, F., Karimi, E., Marrucci, L., de Lisio, C. & Santamato, E. Generation and dynamics of optical beams with polarization singularities. *Opt. Express* **21**, 8815–8820 (2013).

[38] Maji, S., Jacob, P. & Brundavanam, M. M. Geometric phase and intensity-controlled extrinsic orbital angular momentum of off-axis vortex beams. *Phys. Rev. Applied* **12**, 054053 (2019).

[39] Sernelius, B. E. *Surface Modes in Physics* (Wiley-VCH Verlag GmbH & Co. KGaA, Weinheim, FRG, 2001).

[40] Kondakci, H. E. & Abouraddy, A. F. Optical space-time wave packets having arbitrary group velocities in free space. *Nat. Commun.* **10** (2019).

[41] Needham, T. *Visual Complex Analysis* (Oxford University Press, Oxford, 1999).

[42] Guo, Y. *et al.* Supersonic rotation of a superfluid: A long-lived dynamical ring. *Phys. Rev. Lett.* **124**, 025301 (2020).

[43] Clerici, M. *et al.* Observation of image pair creation and annihilation from superluminal scattering sources. *Sci. Adv.* **2**, e1501691–e1501691 (2016).

[44] Parkin, S., Knöner, G., Nieminen, T. A., Heckenberg, N. R. & Rubinsztein-Dunlop, H. Measurement of the total optical angular momentum transfer in optical tweezers. *Opt. Express* **14**, 6963 (2006).

[45] Beckley, A. M., Brown, T. G. & Alonso, M. A. Full Poincaré beams. *Optics Express* **18**, 10777 (2010).